NASA/TM–2012-217785

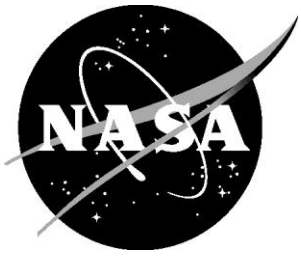

Development and Calibration of a System-Integrated Rotorcraft Finite Element Model for Impact Scenarios

Martin S. Annett, Lucas G. Horta, and Karen E. Jackson
Langley Research Center, Hampton, Virginia

Michael A. Polanco and Justin D. Littell
ATK Space Systems, Hampton, Virginia

November 2012

NASA STI Program . . . in Profile

Since its founding, NASA has been dedicated to the advancement of aeronautics and space science. The NASA scientific and technical information (STI) program plays a key part in helping NASA maintain this important role.

The NASA STI program operates under the auspices of the Agency Chief Information Officer. It collects, organizes, provides for archiving, and disseminates NASA's STI. The NASA STI program provides access to the NASA Aeronautics and Space Database and its public interface, the NASA Technical Report Server, thus providing one of the largest collections of aeronautical and space science STI in the world. Results are published in both non-NASA channels and by NASA in the NASA STI Report Series, which includes the following report types:

- TECHNICAL PUBLICATION. Reports of completed research or a major significant phase of research that present the results of NASA Programs and include extensive data or theoretical analysis. Includes compilations of significant scientific and technical data and information deemed to be of continuing reference value. NASA counterpart of peer-reviewed formal professional papers, but having less stringent limitations on manuscript length and extent of graphic presentations.

- TECHNICAL MEMORANDUM. Scientific and technical findings that are preliminary or of specialized interest, e.g., quick release reports, working papers, and bibliographies that contain minimal annotation. Does not contain extensive analysis.

- CONTRACTOR REPORT. Scientific and technical findings by NASA-sponsored contractors and grantees.

- CONFERENCE PUBLICATION. Collected papers from scientific and technical conferences, symposia, seminars, or other meetings sponsored or co-sponsored by NASA.

- SPECIAL PUBLICATION. Scientific, technical, or historical information from NASA programs, projects, and missions, often concerned with subjects having substantial public interest.

- TECHNICAL TRANSLATION. English-language translations of foreign scientific and technical material pertinent to NASA's mission.

Specialized services also include organizing and publishing research results, distributing specialized research announcements and feeds, providing information desk and personal search support, and enabling data exchange services.

For more information about the NASA STI program, see the following:

- Access the NASA STI program home page at *http://www.sti.nasa.gov*

- E-mail your question to help@sti.nasa.gov

- Fax your question to the NASA STI Information Desk at 443-757-5803

- Phone the NASA STI Information Desk at 443-757-5802

- Write to:
  STI Information Desk
  NASA Center for AeroSpace Information
  7115 Standard Drive
  Hanover, MD 21076-1320

NASA/TM–2012-217785

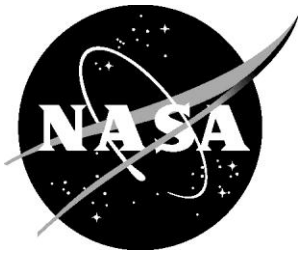

Development and Calibration of a System-Integrated Rotorcraft Finite Element Model for Impact Scenarios

Martin S. Annett, Lucas G. Horta, and Karen E. Jackson
Langley Research Center, Hampton, Virginia

Michael A. Polanco and Justin D. Littell
ATK Space Systems, Hampton, Virginia

National Aeronautics and
Space Administration

Langley Research Center
Hampton, Virginia 23681-2199

November 2012

Available from:

NASA Center for AeroSpace Information
7115 Standard Drive
Hanover, MD 21076-1320
443-757-5802

Abstract

Two full-scale crash tests of an MD-500 helicopter were conducted in 2009 and 2010 at NASA Langley's Landing and Impact Research Facility in support of NASA's Subsonic Rotary Wing Crashworthiness Project. The first crash test was conducted to evaluate the performance of an externally mounted composite deployable energy absorber (DEA) under combined impact conditions. In the second crash test, the energy absorber was removed to establish baseline loads that are regarded as severe but survivable. The presence of this energy absorbing device reduced the peak impact acceleration levels by a factor of three.

Accelerations and kinematic data collected from the crash tests were compared to a system-integrated finite element model of the test article developed in parallel with the test program. In preparation for the full-scale crash test, a series of sub-scale and MD-500 mass simulator tests were conducted to evaluate the impact performances of various components and subsystems, including new crush tubes and the DEA blocks. Parameters defined for the system-integrated finite element model were determined from these tests. Results from 19 accelerometers placed throughout the airframe were compared to finite element model responses.

The model developed for the purposes of predicting acceleration responses from the first crash test was inadequate when evaluating more severe conditions seen in the second crash test. A newly developed model calibration approach that includes uncertainty estimation, parameter sensitivity, impact shape orthogonality, and numerical optimization was used to calibrate model results for the full-scale crash test without the DEA. This combination of heuristic and quantitative methods identified modeling deficiencies, evaluated parameter importance, and proposed required model changes.

The multidimensional calibration techniques presented here are particularly effective in identifying model adequacy. Acceleration results for the calibrated model were compared to test results and the original model results. There was a noticeable improvement in the pilot and copilot region, a slight improvement in the occupant model response, and an over-stiffening effect in the passenger region. One lesson learned was that this approach should be adopted early on, in combination with the building-block approaches that are customarily used, for model development and pretest predictions. Complete crash simulations with validated finite element models can be used to satisfy crash certification requirements, potentially reducing overall development costs.

THIS PAGE INTENTIONALLY LEFT BLANK

TABLE OF CONTENTS

LIST OF TABLES

LIST OF FIGURES

Nomenclature

AATD	Aviation Applied Technology Directorate
ACAP	Advanced Composite Airframe Program
ANOVA	analysis of variance
APL	Applied Physics Laboratory
ATD	Anthropomorphic Test Device
CAD	computer aided design
CG	center of gravity
DEA	Deployable Energy Absorber
DOD	Department of Defense
ERBF	Extended Radial Basis Functions
FEM	finite element model
HSTM	Human Surrogate Torso Model
HTFEM	Human Torso Finite Element Model
LandIR	landing and impact research
LSTC	Livermore Software Technology Corporation
MELB	Mission Enhanced Little Bird
NASA	National Aeronautics and Space Administration
OML	outer mold line
SRW	Subsonic Rotary Wing Project

INTRODUCTION

Crashworthiness is the study of a vehicle structure's ability to withstand impact loads by sustaining occupied volume and limiting occupant loads and injury risk. The rotorcraft community is researching and incorporating novel crashworthy features that significantly absorb kinetic energy for impacts ranging from mild to severe-but-survivable. These crashworthy concepts require large inelastic deformations to be effective. For example, airbags and crushable composite cushions are two external energy absorbing systems that can be easily stowed and rapidly deployed without affecting the vehicle operability. Internal systems, including load limiting seats, crushable subfloors, and frangible interfaces, are currently in operation but are limited in effectiveness by available space.

The National Aeronautics and Space Administration (NASA) Subsonic Rotary Wing Project (SRW) has sponsored research to evaluate new materials and structural concepts to improve rotorcraft crashworthiness and to increase occupant survivability. The tasks identified under the SRW project include evaluation of a composite honeycomb Deployable Energy Absorber (DEA) (ref. 1), material parameter uncertainty quantification, occupant modeling, and injury risk assessment. A task was also established to develop and validate a system-integrated rotorcraft finite element model (FEM), which incorporates aspects of the aforementioned tasks. As part of this effort, two full-scale helicopter tests were conducted to study structural concepts for crashworthiness, to develop and validate component models to predict energy absorption performance, and, lastly, to validate system-integrated finite element models. In the first full-scale test, the DEA performance was evaluated. To assess the nominal landing loads, a second full-scale test was conducted that did not include the DEA.

For the Department of Defense (DOD), the standard document for light fixed wing and rotary wing crash resistance, MIL–STD–1290A, details seven crash impact design scenarios and specifies occupant seat acceleration limits and occupied volume reduction constraints (ref. 2). These design conditions are intended to encompass all weight classes and to account for two impact surfaces, rigid and plowed soil. Federal Aviation Regulations specify minimum velocity and velocity rise-time conditions that must be evaluated for occupant protection (ref. 3). The analytical capabilities available when these standards were established were limited; therefore, it was expected that crash testing would be primarily used to determine compliance. Ever since, more crashworthy features have been implemented into designs, more mishap data has been accumulated, and modeling and prediction tools for crashworthiness and injury biomechanics have improved.

Efforts are underway to revisit the existing requirements and generate full spectrum crashworthiness criteria across all DOD services that account for weight class, operating conditions, and impact conditions (ref. 4). Essential in this effort is the development and assessment of modeling tools to relate impact velocities, attitudes, and terrains to seat interface and occupant acceleration loads, commonly known as G-loads. Ultimately, crash safety certification by analysis is sought to lessen the necessity for costly full-scale crash tests. As the technology evolves to efficiently incorporate more modeling and simulation into the design process, next generation rotorcraft will include more crashworthy features without sacrificing performance and minimizing weight increases. Survivability envelopes for a range of velocities,

attitudes, and terrains can be developed from both tests and system-integrated models with a high degree of confidence.

The analytical techniques necessary to reliably assess impact loads are less mature compared with other dynamic analyses required to assess other phases of rotorcraft flight. Highly nonlinear deformation, contact loading, and material response characterize the energy absorption mechanisms of the airframe. The inclusion of all components in a single comprehensive computational model allows for interactions that one might neglect when analyzing systems using uncoupled models. Modeling detailed representations of the airframe, seats, restraints, and occupants into a single FEM is now a common practice within the automotive crashworthiness community (ref. 5 and 6). Prior to the mid 1990s, most impact analyses were sequentially coupled, with vehicle model responses defined as pulse inputs for occupant, seat, and restraint models. Interaction between the vehicle and occupant models required simplifying assumptions. Efforts to conduct integrated simulations have progressed along with advances in computing capability.

Attempts to compare aerospace vehicle-level simulations with full-scale testing originated in the late 1970s with the KRASH analysis program (ref. 7). The airframe structure was represented as a framework of concentrated mass and bar elements, which relied heavily on semi-empirical data to tailor the model response. Cronkhite and Mazza (ref. 8) initially compared a US Army Advanced Composite Airframe Program (ACAP) helicopter crash test to KRASH simulations. Throughout the 1980s, codes that apply explicit time integration techniques to solve transient dynamic problems and provide the capability to handle both material and geometric nonlinearities became commonplace. Jackson et al. (ref. 9) compared simulations with the explicit finite element analysis program MSC/DYTRAN to the ACAP test. KRASH was coupled with MSC/DYTRAN to provide a hybrid computational framework for correlation with UH-1 helicopter water impact tests (ref. 10). Recently, LS-DYNA has become the predominant commercial code for conducting crashworthiness simulations because of its robust contact algorithms and extensive material library (ref. 11). Jackson and Fasanella compared results from a vertical drop test of an ATR42-300 fixed wing commuter aircraft with simulation using LS–DYNA (ref. 12).

Recent advancements in computational techniques have allowed for streamlined and efficient evaluations of the crash performance of rotorcraft. Finite element models have been developed that contain sufficient fidelity to model plastic deformation within the airframe during impact and are yet computationally affordable. Detailed representations of seats, occupants, and restraints are included to account for the load transfer between the airframe and the occupant and to directly assess the likelihood of occupant injury. Allowing for increasingly complex models does not guarantee the accuracy of their predictions. Complementary to the development of any impact finite element model is the process of verification and validation (ref. 13). Verification of models involves determining if the mathematical realization of the equation of motion is accurately implemented. Impact dynamics analyses typically rely on commercial finite element codes. Therefore, it is assumed that verification of the code is accounted for by the code vendor.

The validation phase involves establishing confidence that the model results accurately represent that the physics of the problem over an applicable domain. In addition, model uncertainty must be quantified against the experimental data and be consistent across the entire range of impact

conditions. Full-scale impact tests are costly and infrequently conducted; therefore, identification of valuable validation metrics is vital.

Typically, validation comparisons between test and analysis are both qualitative and quantitative. One qualitative approach, only possible by the use of high-fidelity finite element models, is to compare post-impact airframe deformations and regions of damage. Quantitatively, the assertion of a properly validated model can be first made by comparing error in kinematic responses such as position, velocity, or pitch angle. Any discernible differences that do exist between test and analysis require identifying and adjusting parameters within the model; however, kinematic responses alone may not provide enough insight to guide adjustment. Output time history responses such as acceleration, velocity, strain, and pressure are then compared between sensor locations and their respective model nodes or elements. Relative errors for magnitude, time of arrival, and pulse duration can be used to compute comparison metrics such as Sprague and Geers (ref. 14) and Russell (ref. 15). These metrics can reinforce model adequacy if acceptance criteria are satisfied, but they provide minimal guidance into required modifications to model parameters in the case of significant discrepancies.

Model calibration, or model updating, is undertaken throughout the verification and validation process to infer model parameters that would improve the agreement between the analysis and test results. Calibration based on a sparse set of test data does not imply validation over the entire applicable design space. With additional test results, it can be demonstrated that model calibration successfully validates the model. Test and analysis acceleration responses often contain high frequency oscillations, particularly for thin-walled airframe components under severe impact conditions. Correlating individual time-history magnitudes and durations becomes challenging and ambiguous. Low-pass filtering results may obscure deficiencies in the model that would need to be improved to reconcile test with analysis. An approach is desired that reveals both the temporal and spatial distribution of acceleration responses, taking advantage of the wealth of instrumentation available in full-scale tests. The approach initially discussed by Horta in (ref. 16) is used when calibrating specific airframe parameters to crash test results.

Development of the system-integrated FEM was predicated on a series of tests, ranging from the component level to the culminating full-scale crash test. These component tests included quasi-static and dynamic loading of a crush tube shock strut, seat mesh impact testing, coefficient of friction testing, and MD-500 mass simulator swing tests. An independent calibration effort was performed for the model of a Hybrid III Anthropomorphic Test Device (ATD) (ref. 17). A series of rigid seat drop tests with Hybrid II and Hybrid III ATDs were used to improve model responses in the pelvic region of the Hybrid III FEM. The fully calibrated model is executed for both crash test conditions, encompassing a design space and loading that extends from benign to severe.

Finite element analyses of these ATD tests were also performed in parallel. This hierarchical approach expanded confidence and mitigated uncertainties in component representation within the FEM. Airframe calibration is conducted based on results from the second full-scale crash test. For calibration, both heuristic and quantitative methods are used to identify modeling deficiencies, evaluate parameter importance, and propose required model changes. Calibration requires multiple model simulations with a variety of parameter inputs. Therefore, calibration

approaches are adopted that are computationally affordable yet include sufficient modeling detail.

The report organization is as follows. First, a detailed description of the full-scale crash test program is presented, which includes a description of the facility and a description of the various test configurations and test conditions. Second, a discussion of the pretest model component development is included. In this section components such as the DEA, crush tube analysis and testing, the MD-500 mass-simulator and skid gear analysis and testing, the seat FEM model development, and the Hybrid II and III Anthropomorphic Test Device FEM calibration efforts are presented. Third, a discussion of the MD-500 helicopter analysis and test results with the DEA is provided followed by results without the DEA. Fourth, the model calibration methodology using the test with the DEA is discussed. This discussion is followed by updated results using both test configurations (with and without DEA). Finally, the concluding remarks present a summary of findings and lessons learned.

FULL-SCALE CRASH TEST DESCRIPTION

Full-scale crash tests of the MD-500 helicopter were performed at NASA Langley's Landing and Impact Research Facility (LandIR) in November 2009 and March 2010 (ref. 18). The LandIR facility is a 240 ft tall gantry structure with swing cables attached at one end and a movable pullback platform positioned on the opposite end. Two pullback cables raise the test article to a prescribed height. Upon pyrotechnic release of the pullback cable, the test article swings along two pairs of swing cables attached to the test article. The two pairs of swing cables are equally spaced to form a parallelogram. This configuration controls pitch, roll, and yaw rate during the swing. The swing cables are pyrotechnically severed just prior to impact. Figure 1 shows an aerial view of the facility and a notional schematic of a swing test.

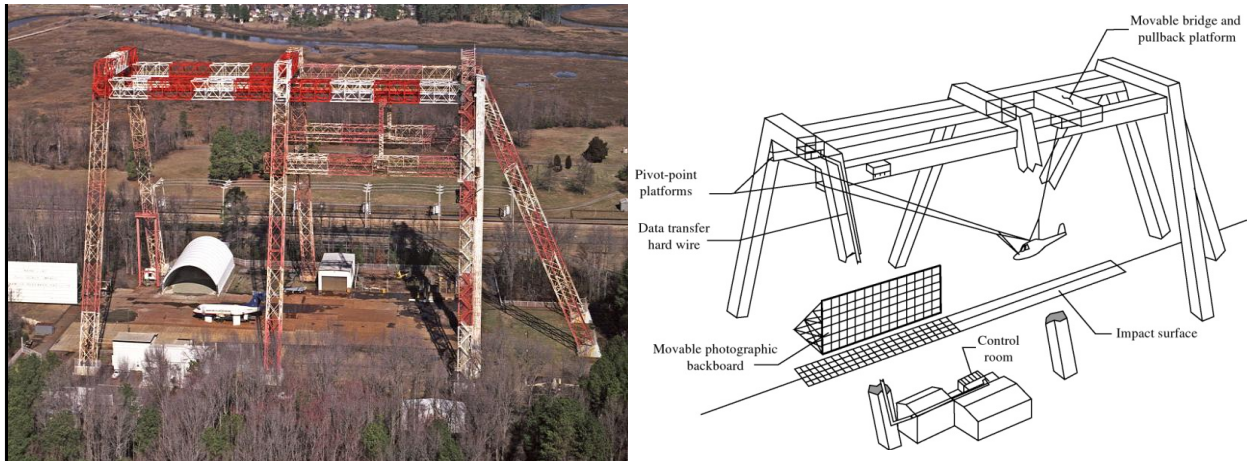

(a) Photograph of LandIR. **(b) Schematic of LandIR.**

Figure 1. NASA Langley Landing and Impact Research Facility.

Target impact conditions were 26 ft/sec vertical and 40 ft/sec horizontal while maintaining zero pitch, roll, and yaw attitude. Although this impact condition is severe, it is still considered survivable. The test was conducted by suspending the helicopter from the gantry structure using two sets of cables: pullback cables and swing cables. These cables were attached to the airframe at hard points that enabled the helicopter to be lifted through its center of gravity (CG).

An MD-500 airframe was provided by the US Army's Mission Enhanced Little Bird (MELB) program. Variants of this helicopter, including the OH-6 and the MD-530, have been flown in civilian and military applications for more than 40 years. A photograph of the MD-500E helicopter, manufactured by MD Helicopters, Inc. of Mesa, Arizona, is shown in Figure 2a. Currently the MD-500 is used as a general purpose utility and executive transport helicopter for both military and civilian applications. The MD-500 helicopter is designed to seat four occupants, two crew and two passengers. The test article is shown in Figure 2b. Occupants were placed in standard civilian-issue seats and restrained using four point harnesses for the crew and three point harnesses for the passengers. Seats consisted of a framework of aluminum tubing and nylon mesh fabric stretched over the frames to form a seat pan and seat back.

(a) MD-500E helicopter.

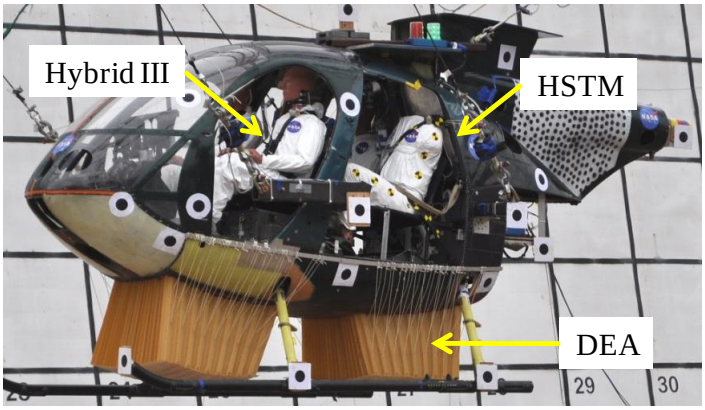

(b) MD-500 crash test article with two DEA blocks attached.

Figure 2. MD-500 helicopter.

The target mass for the test article was set to 2,900 lb, which is roughly the maximum gross takeoff weight for the MD-500E. The empty weight was approximately 500 lb. Ballast mass was distributed onto the test article by adding steel tubing for swing cabling fixtures, steel plates and tubing to represent rotor and tail mass, and data acquisition support hardware to represent the transmission. Sand bags were placed in the subfloor region to account for fuel mass. The total weights of the test article with and without the DEA were 2,940 lb and 2,906 lb, respectively. The weight and balance information was determined prior to the tests.

Four instrumented ATDs were used to represent two crew and two passengers. The pilot in the front left crew position was a 50th percentile Hybrid III male ATD with a straight lumbar spine similar to the Hybrid II. The copilot in the front right crew position was a 50th percentile Hybrid II male ATD, and the rear passenger on the left side was a 50th percentile Hybrid II male ATD. The Hybrid II and III ATDs weigh 180 lb. For the right rear passenger a specialized Human Surrogate Torso Model (HSTM) developed by The Johns Hopkins University Applied Physics Laboratory (APL) was used (ref. 19). This biofidelic HSTM contains detailed representations of thoracic organs, skeletal structure, and soft tissue and is mated to the pelvis and legs of a 50th percentile Hybrid III male ATD. The weight of the HSTM/Hybrid III ATD is 170 lb.

The critical component evaluated in the first impact test was the externally mounted DEA, which was conceived and patented by Dr. Sotiris Kellas of NASA LaRC (ref. 20). The DEA is a Kevlar-129 fabric/epoxy design that consists of multiple hexagonal cells. The cell wall flat facet

width is one inch and the heights vary from 16 to 20 inches. Two DEA's blocks, spanning the fuselage belly surface, were secured to the fuselage outer skin with parachute cord, which was restrained to the fuselage with two aluminum rails mounted below the door openings. The flexible honeycomb design allows for the DEA to be stowed nearly flat external to the fuselage belly and to be deployed into the hexagonal configuration as notionally shown in Figure 3a. In this configuration, the DEA is loaded along the cell normal axis causing the cell to permanently deform under load and thereby absorb energy. When loaded, the cell walls fold to form a controlled accordion-like pattern (see Figure 3b). Effectiveness of the DEA was evaluated using a building-block approach beginning with material coupon static tests, progressing to sub-component static and dynamic tests, and culminating with the full-scale crash tests.

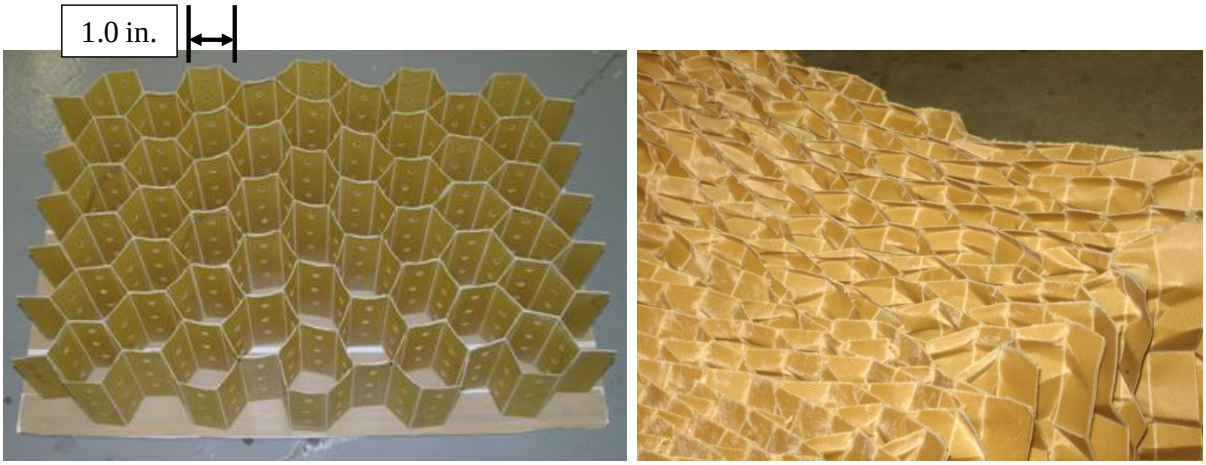

(a) DEA in deployed configuration. **(b) Post-impact DEA deformation.**

Figure 3. DEA concept.

The MD-500 standard oleo-pneumatic struts, mounted between the skid gear and the airframe, are rated for 6 feet-per-second vertical impact conditions. With the high impact velocities expected in the full-scale crash, the airframe hard points were likely to be overloaded as the struts bottom out and become rigid under the high impact velocities expected in the full-scale crash test. Consequently, the oleo-pneumatic struts were replaced with a set of crush tubes to absorb energy through inversion drawing. The crush tubes allow the skid gear to properly swing out on impact without being overloaded. The tubes are overwrapped with graphite/epoxy, which strengthens the column buckling strength beyond the crush load. Rod ends are attached at either end of the tube to impose purely axial loads through the strut length. The crush tube design is shown in Figure 4.

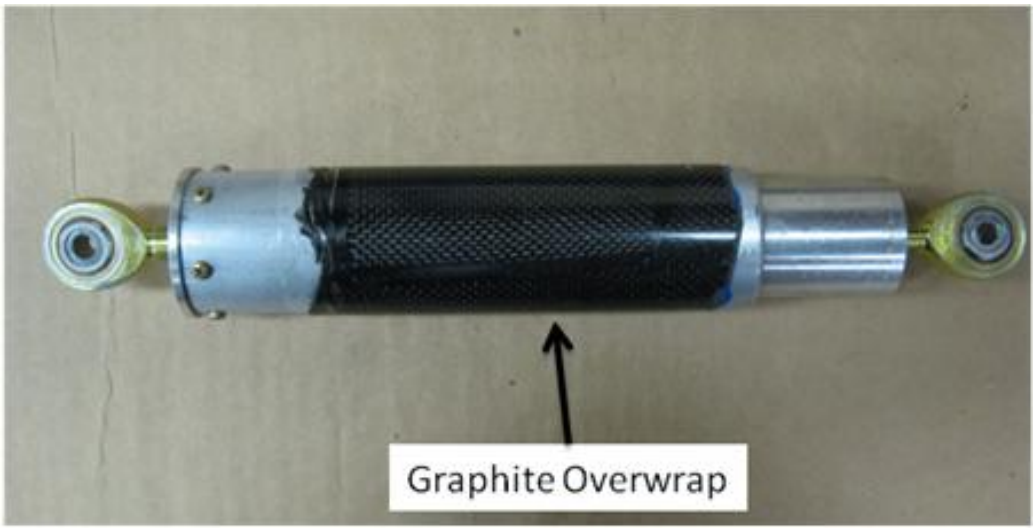

Figure 4. Vertical struts.

For instrumentation the fuselage and skid gear used a combination of strain gages and accelerometers. ATD instrumentation includes head, chest, and pelvic accelerometers, lumbar load cells, restraint load cells, and pressure gages. Data, totaling 160 channels, were collected at a sample rate of 10,000 Hz. Measurements of vehicle kinematics were taken using two and three dimensional large field photogrammetry (ref. 21).

A detailed description of the test results is provided in (ref. 18). The impact conditions for the two full-scale helicopter tests are summarized in Table 1. Note that the pitch, roll, and yaw attitudes for the test with DEA were off-nominal. It was determined that the variations in the distribution of swing cable tension loads prior to release introduced rotational motion upon release. Several prelift tests were conducted prior to the second full-scale crash test to determine proper alignment procedures for cable loads that resulted in impact conditions closer to nominal for roll and yaw.

Table 1. Full-scale test impact conditions.

Test Parameters		Nominal Conditions	MD-500 with DEA	MD-500 Without DEA
Vehicle Weight (lb)		2,900	2,940	2,906
Linear Velocity (ft/sec)	Forward	40.0	38.8	39.1
	Vertical	26.0	25.6	24.1
	Lateral	0	0.5	0.6
Attitude (deg)	Pitch	0	–5.69	–6.2
	Roll	0	7.04	1.9
	Yaw	0	9.3	2.1
Angular Velocity (deg/sec)	Pitch Rate	0	0.44	0.54
	Roll Rate	0	1.11	0.68
	Yaw Rate	0	4.82	1.65

Figure 5 shows test sequence photos for the crash test with the DEA. Picture 5a shows the helicopter approximately 30 ms before impact, pitched down and with some slight yaw. Picture 5b shows the helicopter at the point of first skid gear impact when the right gear touches the ground. Picture 5c shows the point of maximum DEA crushing, and picture 5d shows post-impact rebound. The front right side skid gear impacted the ground first, which was caused by the yaw and roll introduced during the swing. At the point of maximum crushing of the DEA (picture 5c), the helicopter leveled out to show almost no pitch. After the point of maximum crush, the nose pitched forward on rebound, and the Hybrid ATD heads and torsos flailed forward and to the left.

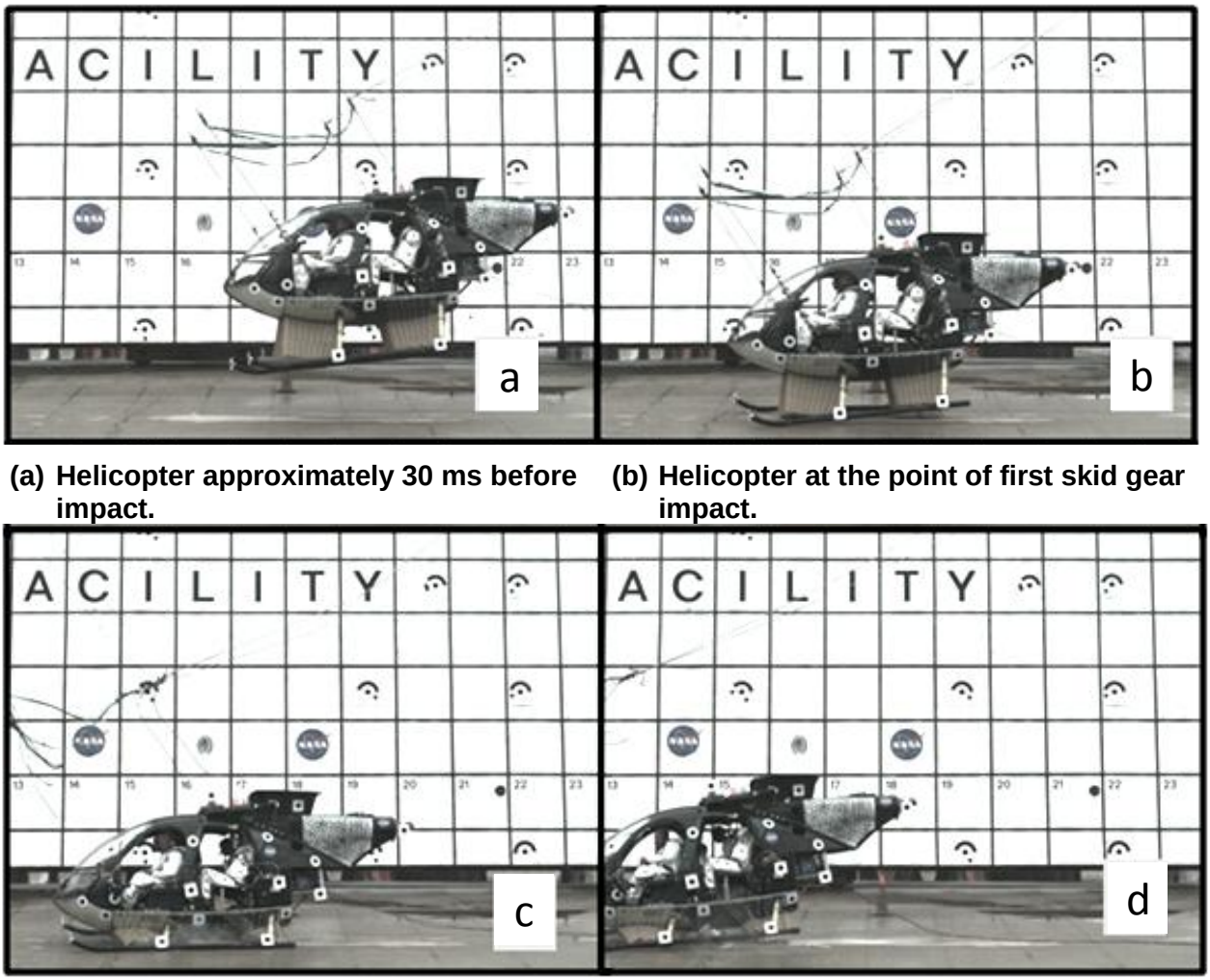

(a) Helicopter approximately 30 ms before impact. **(b) Helicopter at the point of first skid gear impact.**

(c) Point of maximum DEA crushing. **(d) Post-impact rebound.**

Figure 5. Test sequence from south camera, crash test with DEA.

Overall, the damage to the test article was minor. Impact occurred initially on the front right skid gear. Slight tears in the skin above the fuselage opening were evident for both skid gears. The DEA restraint support rail impeded the gear from additional movement that caused the right gear to bend along the rail. Damage along the fuselage belly was limited to the right front section of the belly forward of the front bulkhead. On the other hand, the subfloor and airframe were considered intact, and minimal repair work was required on the forward keel beam and belly to prepare the test article for the crash test without DEA.

Figure 6 shows a sequence of photos for the test without the DEA. Picture 6a shows the helicopter approximately 20 ms before impact. Picture 6b shows the helicopter at the point of first skid gear impact. As with the MD-500 crash test without DEA, the right gear impacted the ground first, but the amount of yaw and roll was lower than the test with the DEA. The fuselage belly impacted the ground approximately 80 ms after gear impact, and the highest vertical deceleration loads were seen thereafter. Picture 6c shows the point of maximum vertical displacement, where the helicopter maintained a slight nose down pitch. Picture 6d shows minor post-impact rebound. After the point of maximum subfloor deformation, the nose pitched forward on rebound, and flailing of the ATD heads and torsos occurred.

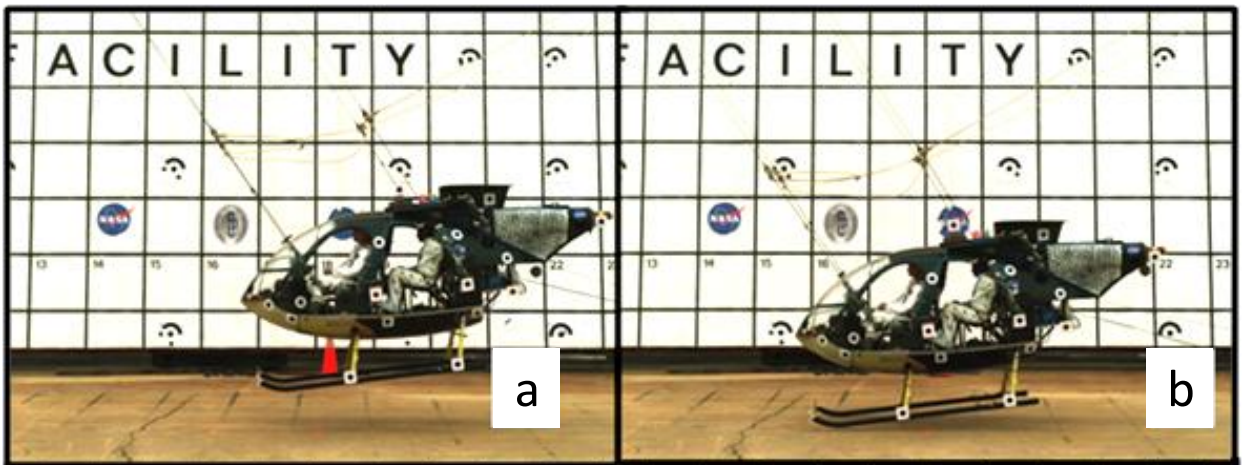

(a) Helicopter approximately 20 ms before impact. **(b) Helicopter at the point of first skid gear impact.**

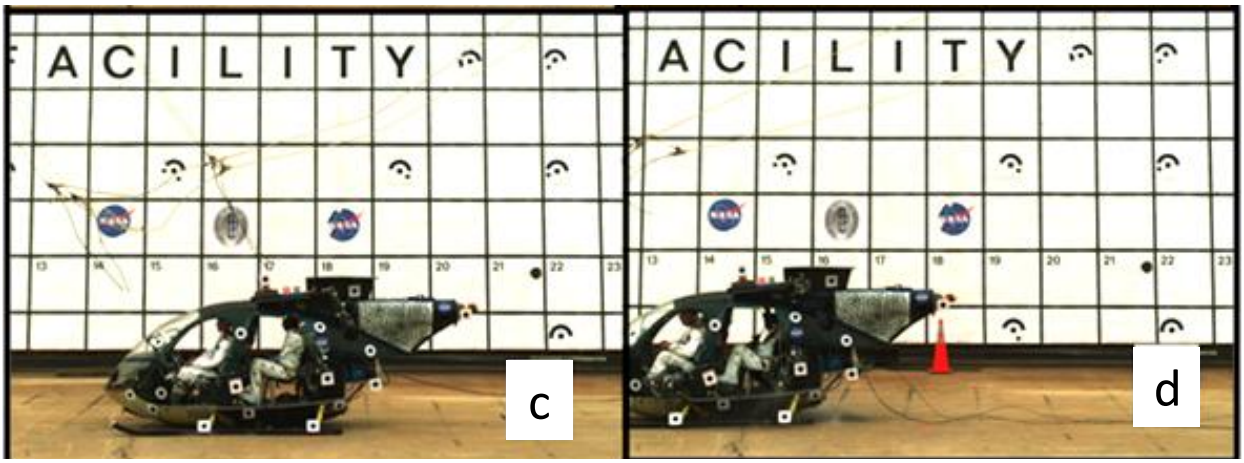

(c) Point of maximum vertical displacement. **(d) Minor post-impact rebound.**

Figure 6. Test sequence from south camera, crash test without DEA.

MODEL COMPONENT DEVELOPMENT

All impact analyses were performed using the explicit nonlinear transient dynamic code LS–DYNA version 971 (ref. 11). LS–DYNA applies explicit time integration techniques to solve transient dynamic problems and provides the capability to handle both material and geometric nonlinearities. All analyses were conducted using shared memory processors (typically four CPUs per run) on a Windows platform.

DEA Model Development

Two fundamental approaches were used to model the DEA. In the first approach, the cell geometry is represented as a continuum with solid elements (ref. 1) and material properties assumed to be elastic-plastic and orthotropic. Material orientation is along the longitudinal axis of the cell wall. With this approach at high volumetric strains, compaction occurs and the slope of the yield stress versus volumetric strain curve in the cell longitudinal direction sharply increases. For the second approach, the cell walls are represented with shell elements that are assigned elastic-plastic and isotropic material properties. The compaction of the DEA is directly replicated as the cell walls plastically hinge and fold (ref. 22). The modeling approaches were evaluated against dynamic crush tests of DEA sections.

The solid based DEA option is attractive since the nonlinearities and crushing response are captured inherently within the material model. Potential users should know that the shell based option requires a large number of elements, when compared to the solid based option, to replicate the folding patterns accurately. Note that nonlinearities in the shell based option are characterized by both geometric and constitutive modeling. The energy attenuation behavior of the solid and shell based DEA models were comparable for vertical only impact conditions. However, when horizontal velocity exists at impact, the solid based model deformation in the in-plane shear direction is not consistent with the test deformations. Furthermore, the crush and deformation patterns differ between the shell and solid based models. In particular, the in-plane response of the shell based model is primarily governed by geometry. Therefore, the collapse of the cell structures and the weak in-plane shear response are intrinsic.

For the shell based models, convergence studies revealed that the maximum acceptable nominal element edge length was approximately 0.3 inches. This dimension corresponds to hundreds of thousands of elements per DEA component. Because adequate computing capacity was available and the solution time was not prohibitive, the shell based model was selected for the system-integrated model. Figure 7a illustrates a typical mesh topology for the shell based DEA model. To model the elastic and piecewise linear plastic behavior of the material, Young's Modulus was set to 340 ksi and initial yield stress to 7,500 psi. Figure 7b shows the plot of the yield stress versus plastic strain curve.

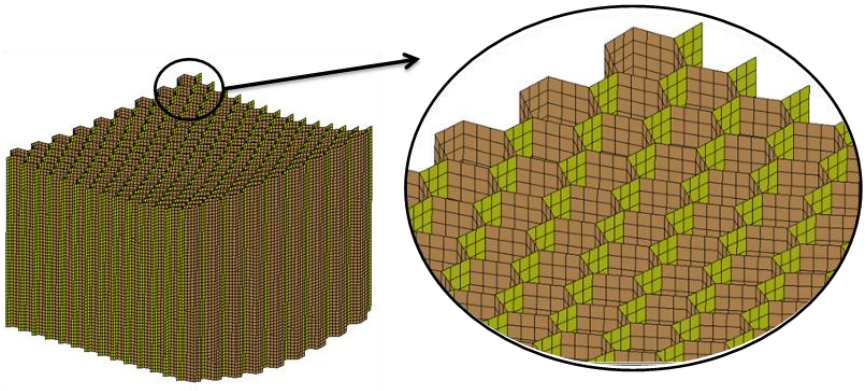

(a) Shell bases DEA FEA.

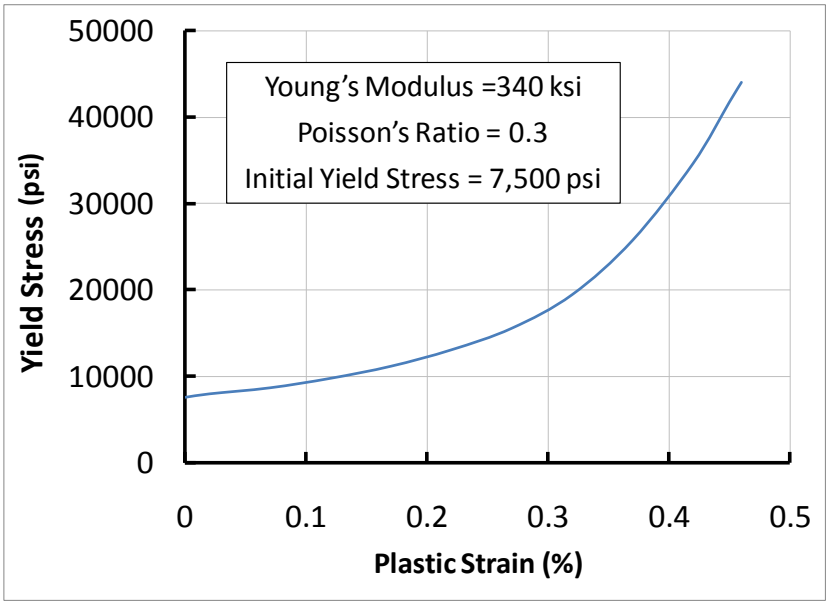

(b) DEA material properties.

Figure 7. DEA FEM.

Skid Gear System Model Development

A critical element of the skid gear is a set of crush tubes, which are modeled as one dimensional truss elements to transfer axial loads to the helicopter frame. Bending loads are introduced into the fuselage when the truss element nodes exceed a rotation angle, and the rod ends come in contact with the surrounding clevises. Data from dynamic impact tests were used to model the stress versus stroke behavior. Figure 8 shows a photograph of the dynamic test setup and a time history of the load. For modeling purposes, the yield stress was defined equivalent to the dynamic crush load of 2,300 lb. A nearly perfectly plastic behavior is assumed upon attaining the crush load.

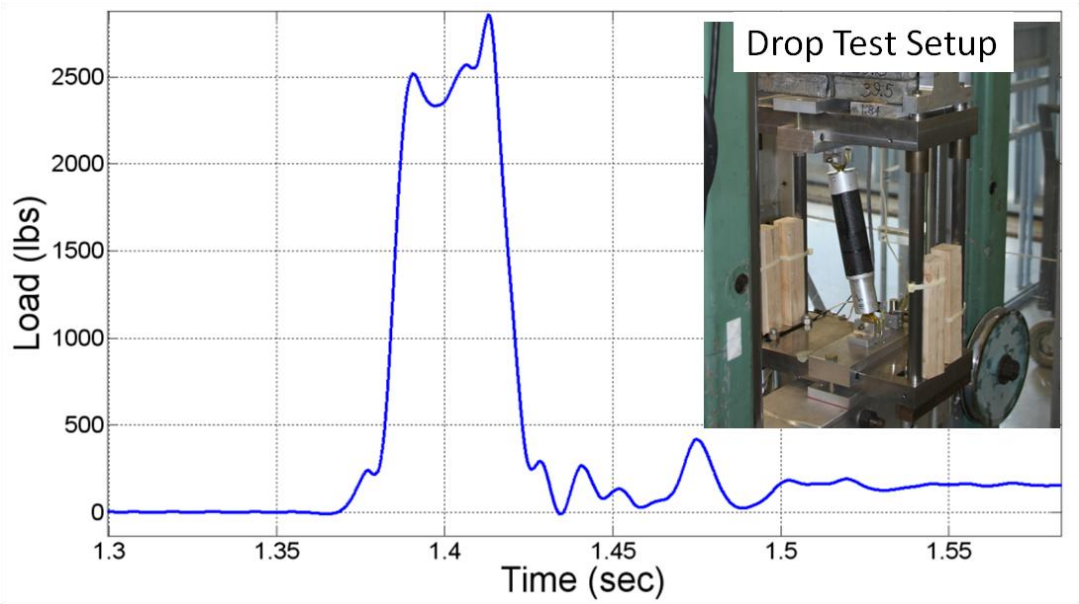

Figure 8. Crush tube dynamic testing.

The skid gear, acquired from an MD-500 parts manufacturer, is composed primarily of Aluminum 7075 T73 die forgings. Each skid gear is attached to a lateral support and hinged along the body centerline. An FEM was created using elastic-plastic shell elements and based on the overall dimensions and wall thickness of the skid gear. Figure 9 shows the skid gear and strut model with a total weight of 80 lbs.

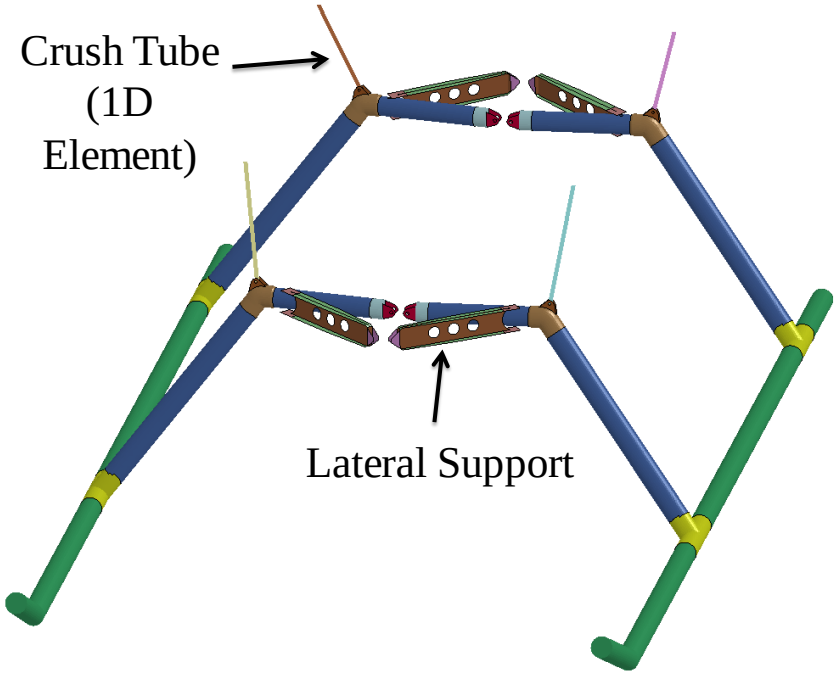

Figure 9. Skid gear FEM.

The performance of the skid gear, crush tubes, and DEA was verified by conducting an impact test of an MD-500 mass simulator. The simulator is a 2,500 lb, 4 in thick aluminum plate attached to the skid gear with stainless steel brackets and lateral supports. It was instrumented with a triaxial accelerometer at the center of gravity and uniaxial strain gages on the vertical tubes of the skid gear. The mass simulator swing test was conducted at the full-scale vertical and horizontal impact velocities of 26 ft/sec and 40 ft/sec, respectively. It included two DEAs approximately 14 inches in height, secured to the underside of the flat plate with parachute cord. Based on results from parametric studies of the DEA (ref. 22), the orientation of the DEA segments was optimized for the specific test impact conditions and set at 20 degrees from vertical. Figure 10 shows both the test article and corresponding FEM.

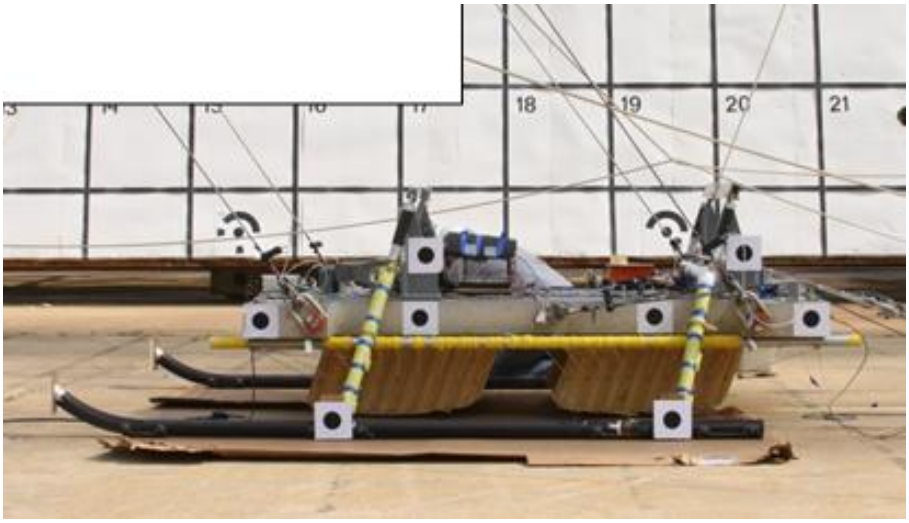

(a) Test article.

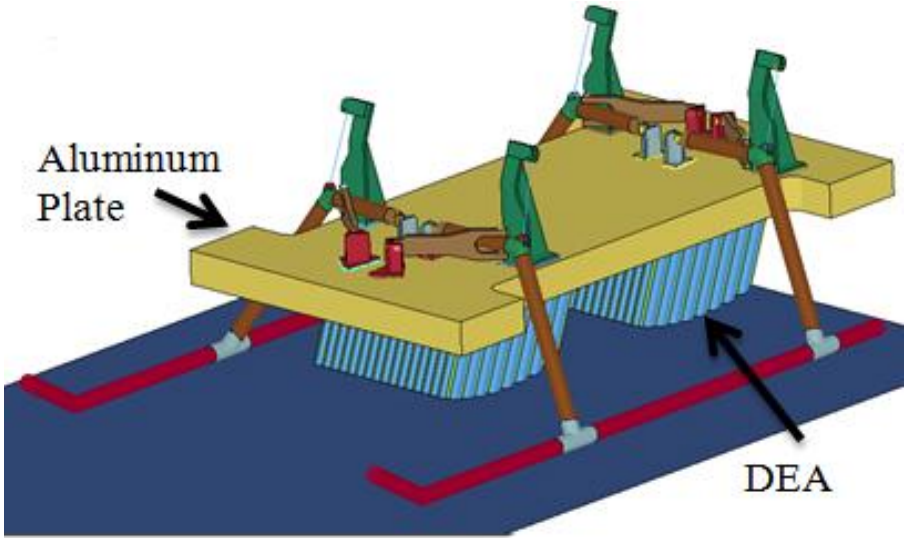

(b) FEM.

Figure 10. MD-500 mass simulator with DEA.

The LS–DYNA model consisted mostly of solid elements for the aluminum plate and brackets. The concrete surface was represented with a planar rigid wall. To model the kinematic interface, the aluminum plate is attached to the gear using brackets and lateral supports hinged and pinned with rigid revolute joints.

Figure 11 shows the vertical and horizontal acceleration responses for both test and analysis. To remove high frequency oscillations from the response, the acceleration data were filtered with a Butterworth 60 Hz low pass filter. Note that the pulse shapes and magnitudes for the vertical acceleration were comparable. However, impact surface friction plays a key role in the behavior of the system during slide out. Therefore, a separate effort was undertaken to conduct independent slow-rate friction drag tests using representative DEA sections. From this test a friction coefficient value 0.5 was computed. However, based on the measured horizontal accelerations, the friction coefficient of 0.5 was too high and had to be reduced to 0.3 for all subsequent simulations with the DEA to provide better correlation.

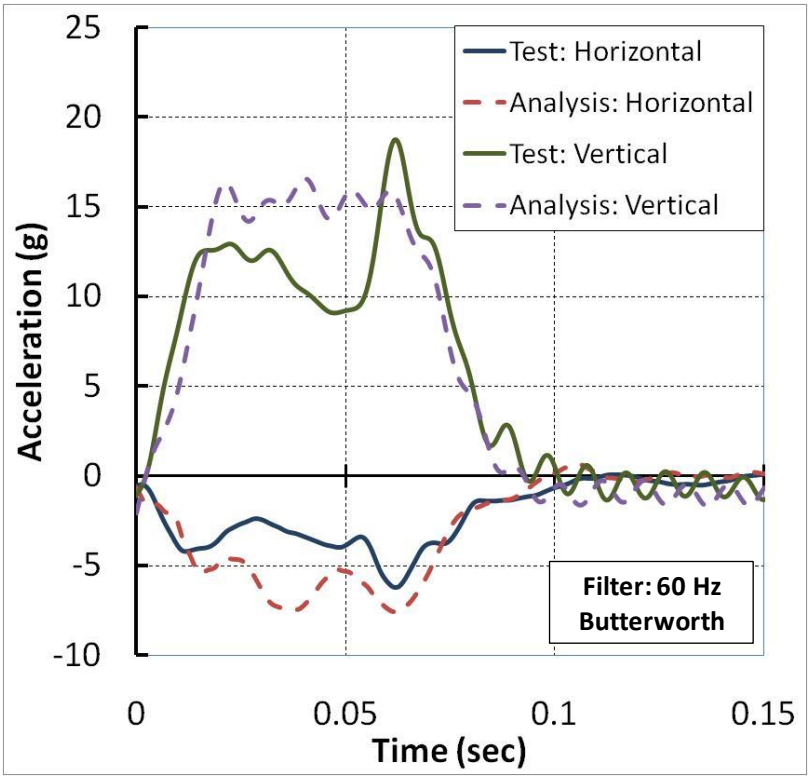

Figure 11. Mass simulator/DEA, test versus analysis comparison, acceleration.

Figure 12 shows test and analysis axial strains for the right forward vertical leg of the skid gear. From these results it is apparent that the vertical members are highly loaded upon impact and exhibit a tension/compression bending response. In spite of this high load, the strains do not exceed the yield allowable for the aluminum, and no plastic deformation was observed from the posttest examination of the skid gear. Because acceleration and strain results compare well between test and analysis, the modeling approach for the skid gear with the crush tubes was deemed adequate.

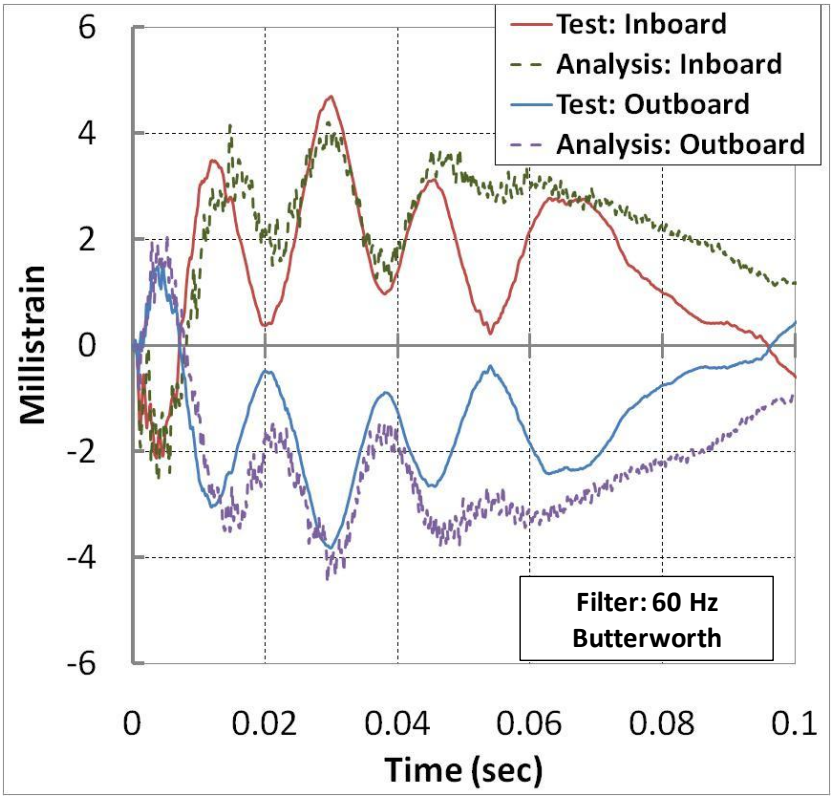

Figure 12. Mass simulator/DEA, test versus analysis comparison, axial strain.

Results from the mass simulator test validated the DEA, skid gear, and crush tube models. In preparation for the full-scale crash test, the remainder of the MD-500 test article was modeled. Attention was given to the components susceptible to damage during impact, namely the fuselage and seats.

Fuselage Model Development

A computer aided design (CAD) model of the MD-500 fuselage was provided by the Army Aviation Applied Technology Directorate (AATD). The geometry model consisted of surface representations of the fuselage outer mold line (OML), bulkheads, seat pan, and floor. A more comprehensive geometry was required that represented the internal primary and secondary structures and could be readily meshed into an FEM. Geometry that contains compatible surface edges eliminates the need to manually manipulate and merge nodes. The model must contain enough detail to represent the expected plastic deformation and accurately transmit loads into the seats and occupants. This underlying geometry provides the foundation for more refined meshing or parameter studies.

Ribs and stiffeners not present in the baseline geometry model were measured and added to the existing geometry. Thickness measurements were taken using ultrasonic transducers and calipers. The skin thicknesses typically ranged from 0.02–0.04 in. The keel beam, a critical shear load path for the subfloor, was added. Material densities were scaled up by as much as 50 percent to account for the mass of additional ribs and stiffeners not discretely modeled.

Figure 13 shows the LS–DYNA FEM of the MD-500 fuselage. To keep the computational time low, the element count for the fuselage was targeted not exceed 500,000 elements, including seats and occupants. The original fuselage model was only 27,000 elements (not including skid gear) and composed of shell elements representing airframe skins, ribs and stiffeners. Refinement was concentrated around the subfloor. Ballast representing rotor mass, tail mass, and fuel was incorporated in the FEM as concentrated mass elements. Other components like the pullback and swing fixtures were added as rigid shells. The platform that supported the DAS was mounted in the tail and also modeled as a rigid shell. Although the original geometry had a blunt nose, the FEM was modified to a chine nose to represent the actual fuselage. Material properties for the fuselage were based on the MD-500 Structural Repair Manual (ref. 23) for Aluminum 2024 and 7075 with elastic-plastic properties. The nose was made from fiberglass and the engine fairing was made from a Kevlar fabric. The fiberglass and Kevlar material properties were estimated.

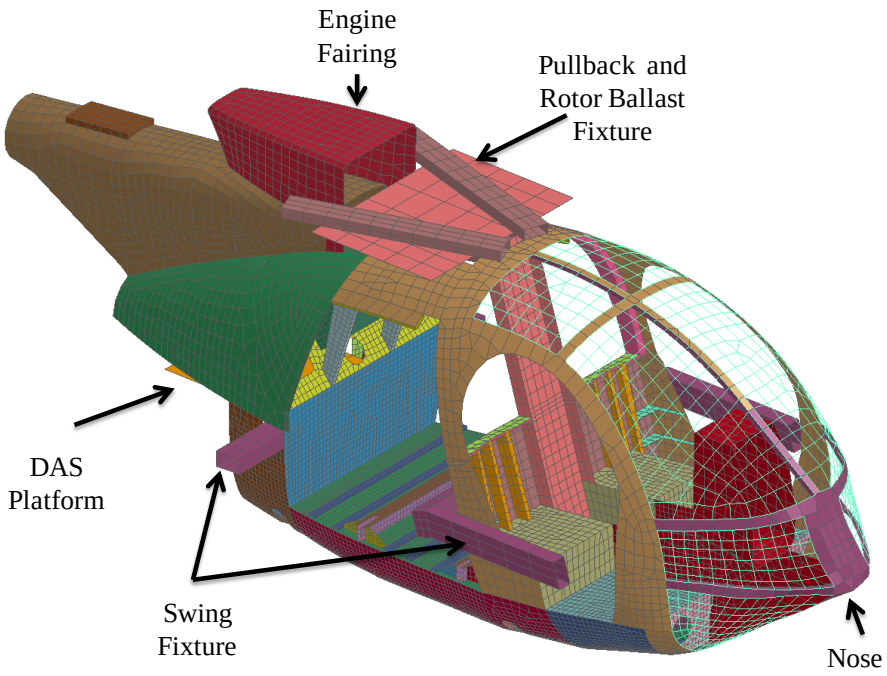

Figure 13. MD-500 fuselage FEM.

Seat Model Development

Two crew seats and a single passenger bench seat were obtained from an MD-500 parts supplier. The seats are standard military issue with aluminum frames and nylon mesh fabric stretched over the frames. Because no geometry was available, the seat geometry was reconstructed using target tracking 3-D photogrammetric techniques. Targets were attached to the seat, and point clouds were generated from images of the targets and converted to parametric solids, which were used to generate a finite element mesh. The as-received passenger bench seat was vulnerable to structural failure at the rear seat pan tubes during impact. Additional support braces, typical of military applications, were added from the front edge of the seat pan to the floor. Rigid links representing this attachment scheme were used in the FEM. The modeling process for the crew seat is illustrated in Figure 14, with both crew seat and passenger bench FEMs included.

Figure 14. MD-500 seats and seat FEMs.

The seat fabric material properties were determined by dynamic drop tests of a 20 lb hemispherical mass onto the fabric. An accelerometer mounted within the drop mass measured the vertical acceleration, which was compared to the FEM simulations. The modulus of the material was modified to match test and analysis accelerations. Figure 15 shows the drop test setup, FEM simulation, and acceleration data comparison. The calculated effective dynamic modulus is 4,000 psi, which exceeded the modulus determined from quasi-static load cell testing by a factor of three.

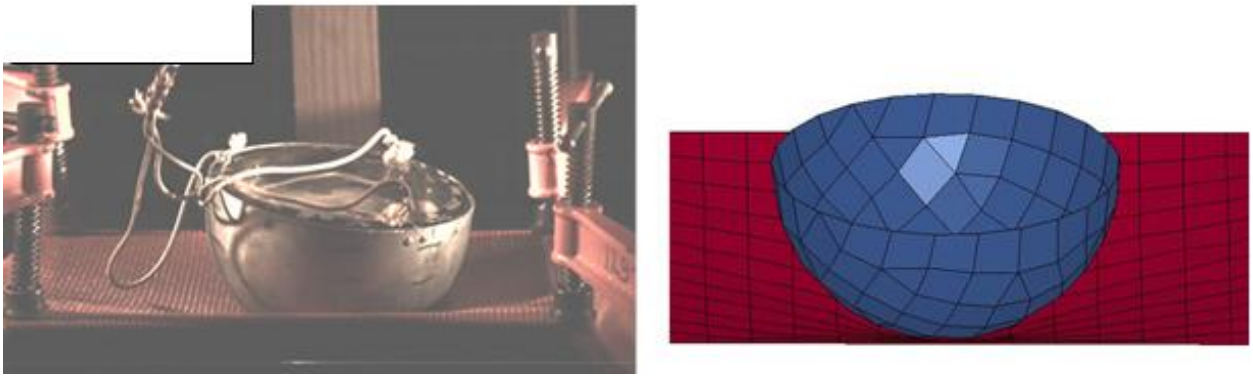

(a) Drop test. (b) FEM.

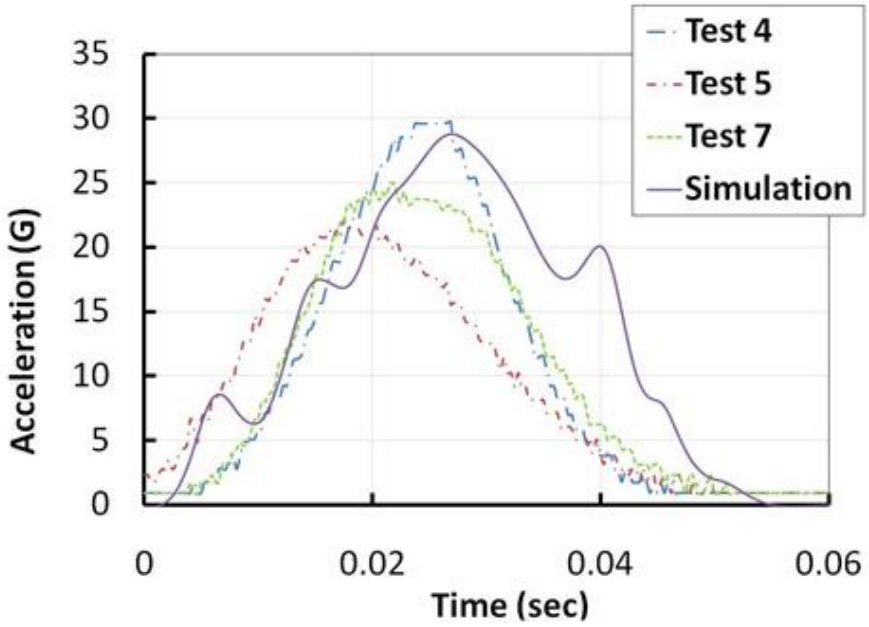

(c) Drop mass acceleration.

Figure 15. Seat mesh dynamic testing.

ATD Model Development

A model of the 50th percentile HYBRID III male was used for the HYBRID II and III ATDs (ref. 24). A third model, provided by the LS–DYNA vendor Livermore Software Technology Corporation (LSTC), is denoted as the LSTC FEM. THE LSTC FEM contains a combination of rigid and deformable discretizations for body parts. Springs and dampers are defined at joints between body parts. Using the LS–DYNA preprocessor, the ATD FEMs are easily imported and positioned within the helicopter model. Figure 16 shows the LSTC FEM containing 4,295 elements with a wide range of element types and joint definitions.

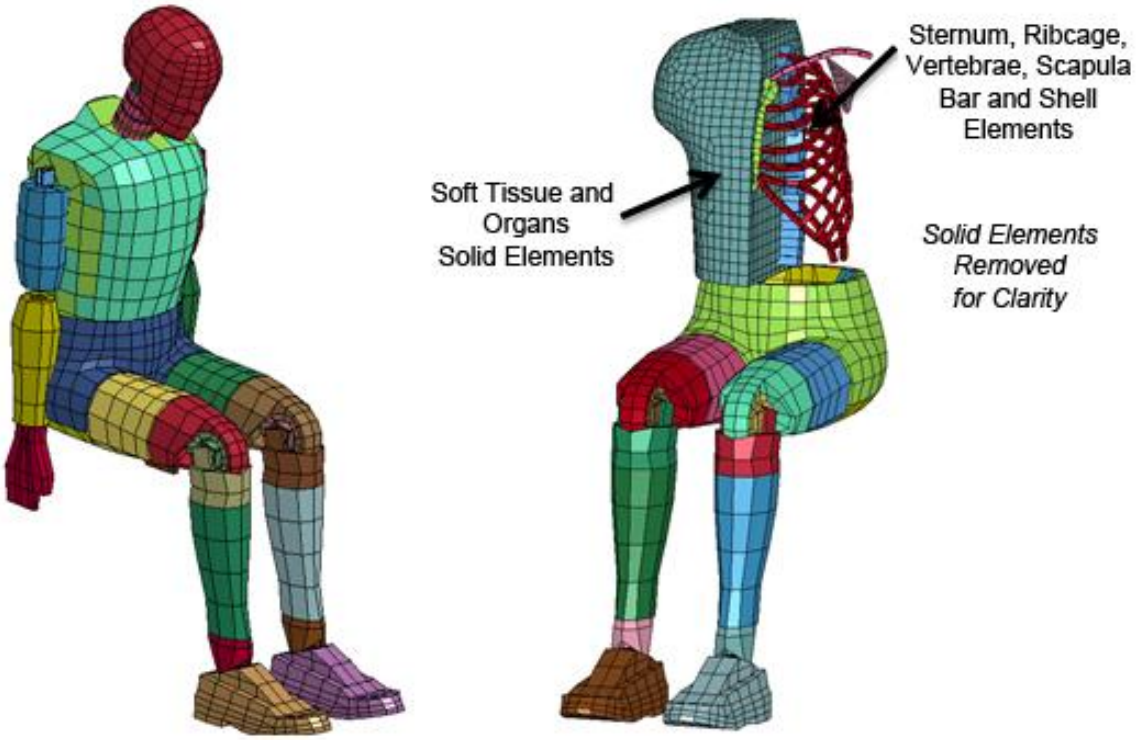

(a) LSTC Hybrid III FEM. **(b) Reduced HTFEM.**

Figure 16. ATD FEMs.

Note that the Hybrid II and III ATDs used in the crash tests are notably different from the LSTC Hybrid III FEM. It is also important to note that the LSTC Hybrid III FEM has been calibrated for automotive frontal impact conditions, with emphasis on capturing head/neck and chest kinematics. For testing in aerospace applications, the Hybrid II and III ATDs contain straight lumbar spines, whereas the LSTC Hybrid III FEM includes the automotive curved spine. Moreover, the LSTC Hybrid III FEM does not contain an abdominal insert, which becomes an important load path from the pelvis to the ribcage under high vertical loading. Therefore, it is understood that the internal responses of the pelvic and lumbar region with the LSTC Hybrid III FEM are not accurate. Results reported in references 17 and 25 support this finding. In cases where shoulder restraints are used, the lack of fidelity in the mass distribution of the LSTC Hybrid III FEM is not as critical because of the limited torso flailing. Capturing the ATD/seat impact, subsequent rebound, and effective mass decoupling is critical for determining the loads in the airframe. The LSTC Hybrid III FEM captures this behavior and is therefore better than using lumped mass representations.

A reduced human torso FEM was constructed and adapted from APL's detailed Human Torso Finite Element Model (HTFEM) (ref. 19). This model includes organs and soft tissue components made from solid silicone elements; and the sternum, ribcage, vertebrae, and scapula are modeled with fiberglass bar and shell elements. The bar and shell elements are embedded within the solid elements and coupled with constraint algorithms. The reduced HTFEM, depicted in Figure 16b, was attached to the LSTC Hybrid III FEM pelvis and legs, and the total model size is 8,034 elements. The pilot and copilot FEMs are restrained with four point harnesses, and

the passenger FEM and reduced HTFEM are restrained with three point harnesses. Seatbelt shell elements were contoured to the torso and pelvis.

Initial System-Integrated Model

The system-integrated MD-500 FEM with the DEA is shown in Figure 17. This original model has approximately 400,000 elements in total, with 266,000 elements representing the DEA. This model size is commensurate with automotive crash model sizes. There are tradeoffs when refining models that use explicit finite element techniques where numerical stability is conditionally enforced if the time steps are sufficiently small. The time step is a function of the shortest element dimension; therefore, for more refined meshes, the time steps decrease and overall runtime increases. For simulation times of 0.2 seconds, the system-integrated MD-500 model runtime is approximately 24 hours.

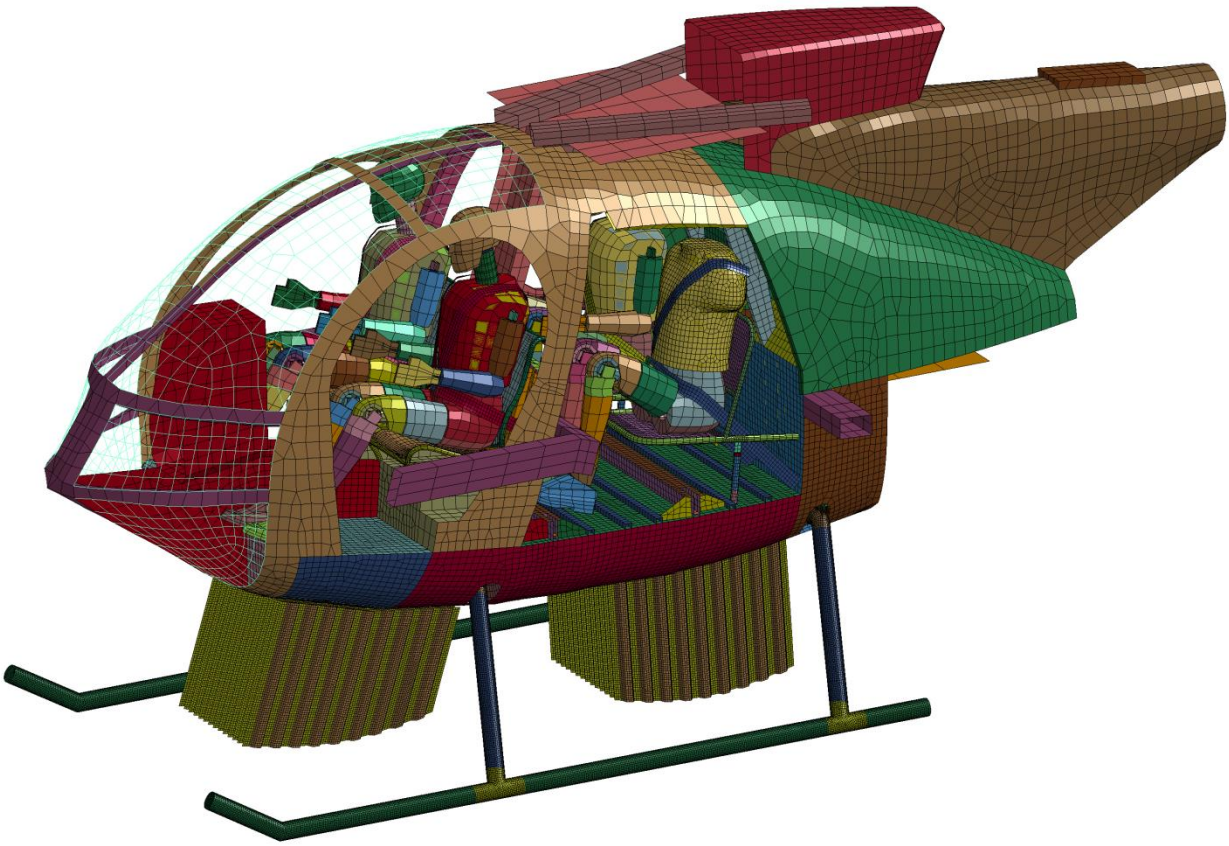

Figure 17. MD-500 system-integrated FEM.

TEST/ANALYSIS RESULTS: CRASH TEST WITH DEA

Figure 17 shows the impact orientation and deformation at peak load for test and analysis. Qualitatively, the global deformation pattern of the deployable energy absorber was similar to the deformation observed from the high speed video, primarily folding on the right side and crushing on the left side, relative to the passenger's view. Consequently, higher impact loads were transferred at locations where the DEA cells simply buckled. However, because damage to the front right side was not evident in the analysis, these regions of folding and crushing do not correspond between test and analysis. Within the simulation, dimpling of the skin occurred in the region above the rear DEA, whereas the posttest inspection revealed no damage. The indiscriminate behavior of DEA folding, crushing, and sliding along the belly was due to the presence of roll attitude and combined lateral and longitudinal loading and was only partly captured with the shell-based DEA model.

(a) Test article prior to impact. **(b) Test article at peak acceleration.**

Figure 18. MD-500 FEM deformation, crash test with DEA.

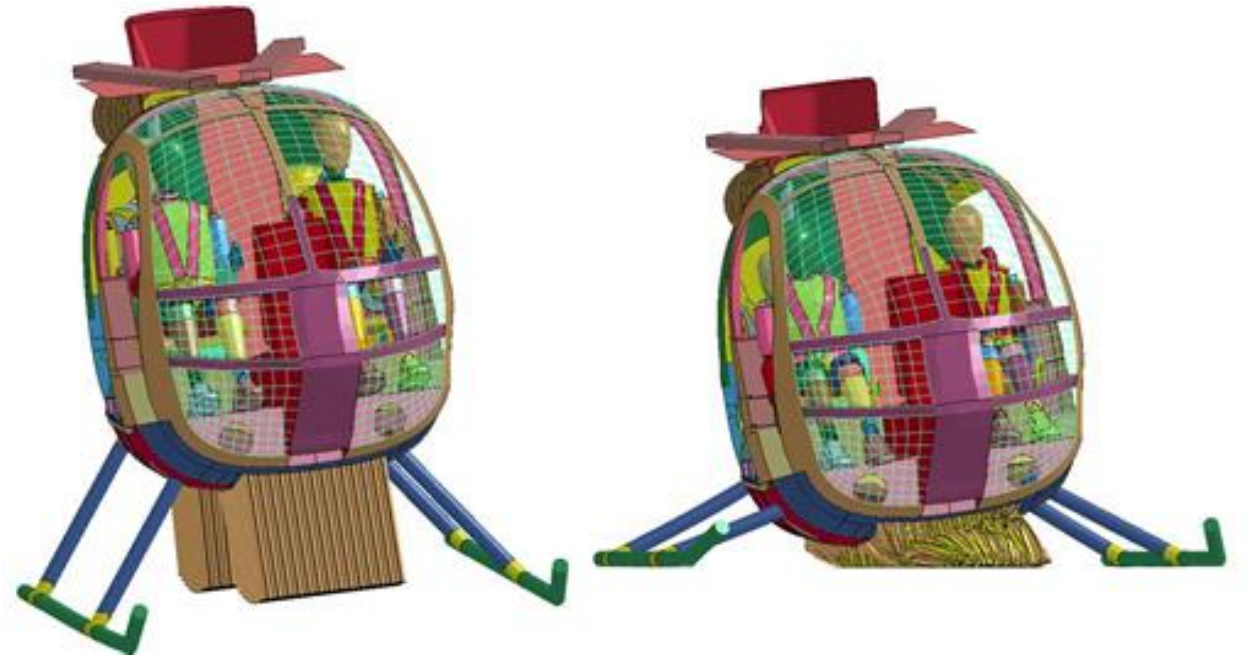

(c) FEM prior to impact. **(d) FEM at peak acceleration.**

Figure 18. Concluded.

Despite the qualitative differences between local deformation patterns, the overall response of the airframe is in reasonable agreement. Nodal accelerations at two critical locations, the pilot seat box and the centerline of the floor beneath the passenger seats, are compared to accelerometer output. The reference coordinate system for the simulation and the test is fixed along the floor surface. The axis perpendicular to the floor represents the vertical direction. For purposes of evaluation of occupant injury criteria such as Eiband, Dynamic Response Index, and Brinkley (ref. 26–28), the responses for the pilot seat box and passenger floor are used as inputs.

Comparisons for acceleration and velocity are plotted for 0.2 seconds, and acceleration signals are low-pass filtered with a second-order Butterworth 60 Hz filter. The pilot seat box vertical accelerations are plotted in Figure 19, and the changes in vertical velocity are plotted in Figure 20. At t = 0, the skid gear initially impacts the surface. At t = 30 ms, the DEA begins to attenuate energy. As expected from previous testing of the DEA, the vertical acceleration waveforms of the airframe are effectively trapezoidal with durations of roughly 0.12 seconds from test and 0.10 seconds from analysis. Note that the DEA performs as a load limiting shock absorber, regulating the loads between 10 and 15 g and expanding the deceleration pulse duration through crushing and folding. Two differences in the pilot seat box response are evident. The test change in velocity approximates the velocity at impact (~26 ft/sec); therefore, there was no rebound in the test article. In the analysis, the change in velocity is greater than the velocity at impact by more than 4 ft/sec, indicating that the simulation shows a rebound. Second the analysis does not show an abrupt increase in the acceleration attributed to compaction of the DEA. In the simulation, the airframe rebounded before considerable compaction of the DEA could occur.

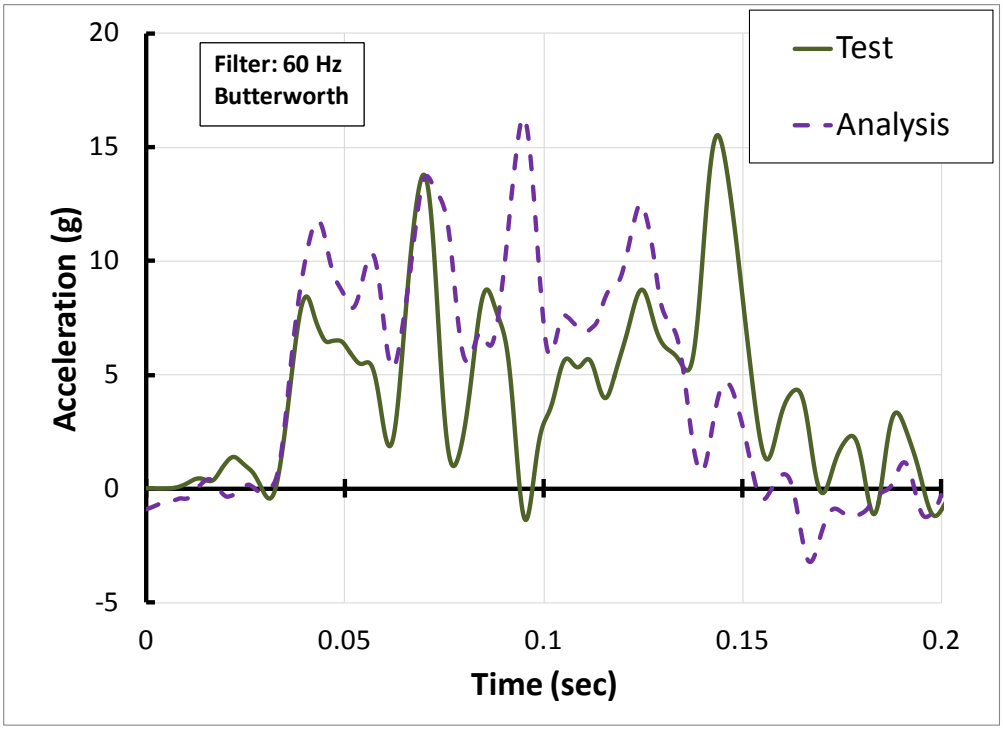

Figure 19. Comparison of test and analysis, pilot seat box vertical acceleration; crash test with DEA.

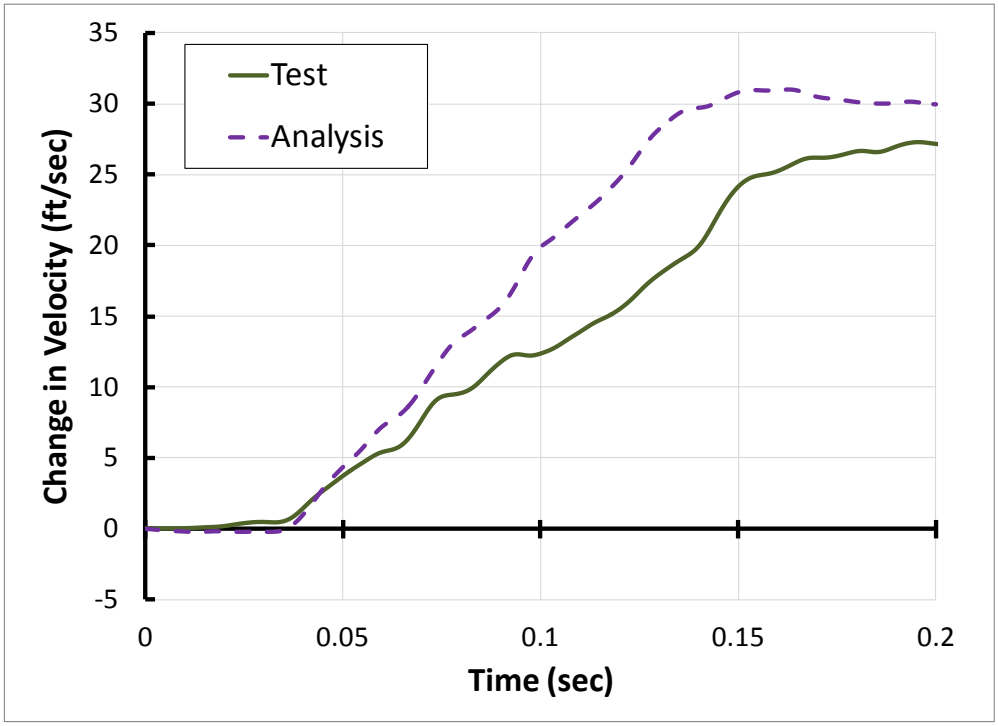

Figure 20. Comparison of test and analysis, pilot seat box vertical change in velocity; crash test with DEA.

The passenger floor accelerations are plotted in Figure 21, and the changes in vertical velocity are plotted in Figure 22. The differences in acceleration pulse duration and velocity rebound are consistent with the pilot seat box responses. The rebounding behavior in the model could be attributed to whether all energy attenuating mechanisms are represented within the DEA shell elements, to contact with the DEA, or to overall interaction of the DEA interface with the belly. However, adjustments of the model to better correlate to the test data appear workable.

Figure 23 shows the predicted and experimental pilot pelvic vertical acceleration. The peak acceleration from the analysis is over twice that seen in the test and the pulse shape is also different. These results provided the first indication that the ATD models were not specifically calibrated for the dominant vertical loading environments experienced in a rotorcraft crash.

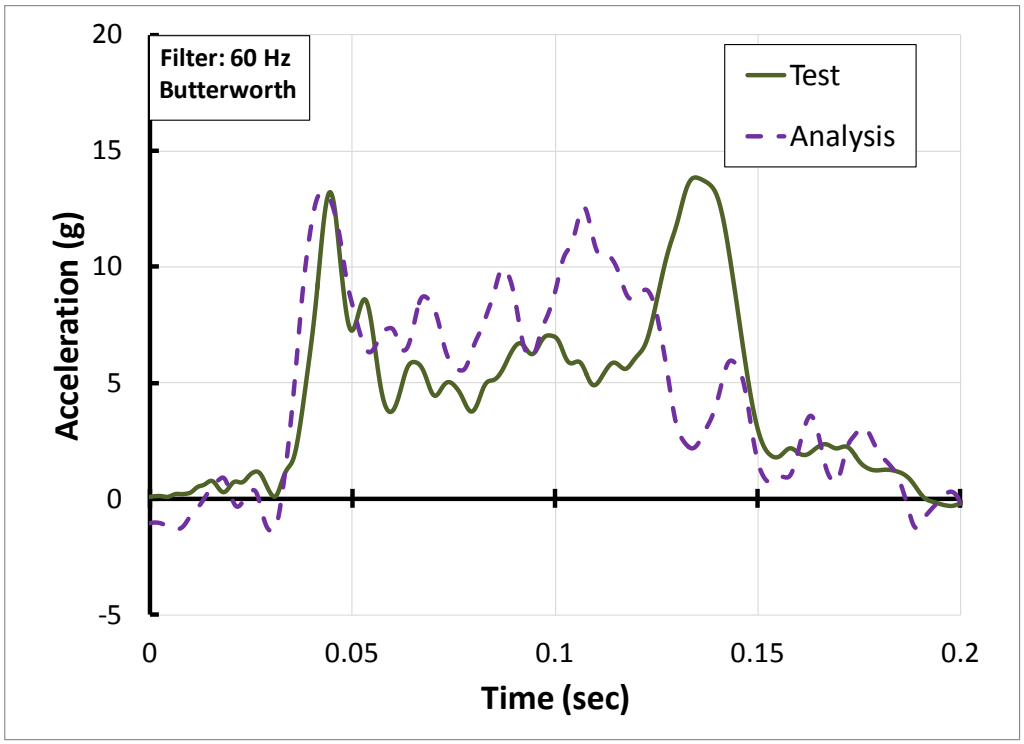

Figure 21. Comparison of test and analysis, passenger floor vertical acceleration; crash test with DEA.

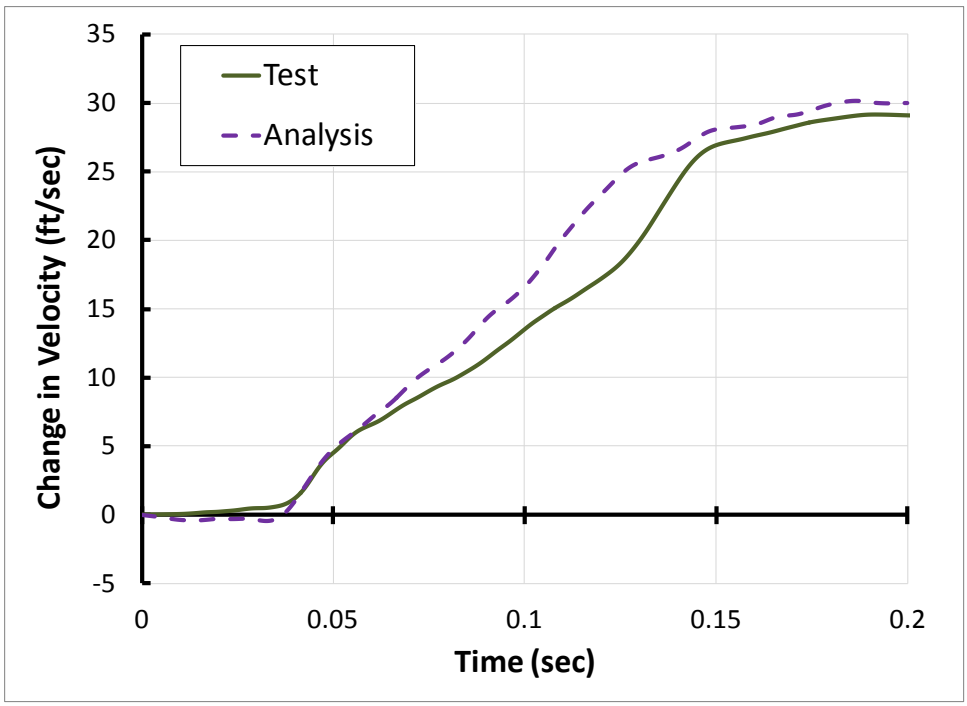

Figure 22. Comparison of test and analysis, passenger floor change in vertical velocity; crash test with DEA.

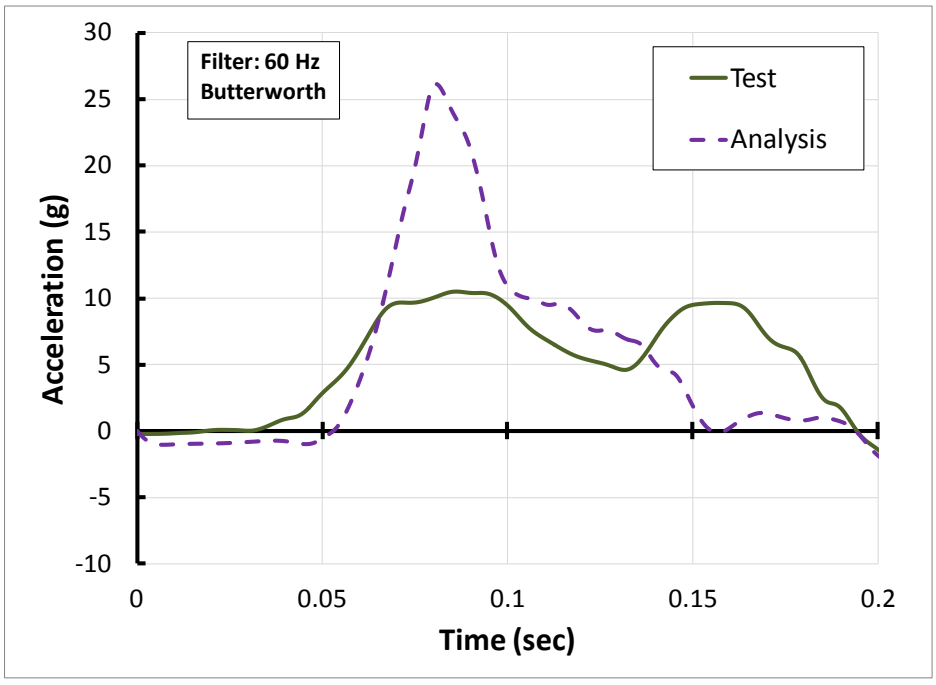

Figure 23. Comparison of test and analysis, pilot pelvis vertical acceleration; crash test with DEA.

TEST/ANALYSIS RESULTS: CRASH TEST WITHOUT DEA

The impact orientation and deformation at peak load is shown for test and analysis in Figure 24. Initial runs of the system-integrated FEM following the crash test without the DEA revealed key shortcomings in the FEM that were not evident when validating against the crash test with DEA. During the test, much of the subfloor secondary structure, including the keel beam and frames, exhibited structural failure. Pilot and copilot seat boxes were permanently deformed, and seat frames either buckled or failed in bending. Furthermore, the tail deformed significantly, and the forward swing cable fixture became dislodged at its interface to the bulkhead. Acceleration magnitudes increased by a factor of three, and pulse durations were reduced to around 0.040 seconds. The pulses were triangular in shape but contained different peaks depending on airframe location.

(a) Test article prior to impact. **(b) Test article at peak acceleration.**

Figure 24. MD-500 FEM deformation, crash test without DEA.

(c) FEM prior to impact. **(d) FEM at peak acceleration.**

Figure 24. Concluded.

Results from the airframe FEM showed that the subfloor mesh was too coarse to accurately capture the keel beam and subfloor frame deformation. The predicted tail deformation was overly compliant compared with the observed tail deformation. This behavior was attributed to a lack of detail, such as omitted frames and stiffeners. To correct for these modeling deficiencies, the subfloor and tail FEM were modified in terms of detail and mesh refinement that resulted in an increased number of airframe elements from 134,000 to 250,000.

Despite some improvements in the FEM, there were inconsistencies in the accelerometer data. These inconsistencies are highlighted when examining measured and predicted pilot seat box and floor vertical accelerations in Figure 25 and change in velocities in Figure 26. The critical impact phase occurred between 0.07–0.13 seconds. The pilot seat box and floor acceleration pulse shapes and magnitudes differed between test and analysis. In addition, the test data show an abrupt spike of 60–70 g on the seat box and the floor, most likely from buckling and failure of the keel beam and shear panel under the seat box. This peak is not seen in the predicted seat box response that has a peak of approximately 30 g. Also, there is a spike of nearly 50 g in the predicted floor response, but the timing is not coincident. The analytical change in velocities for the floor is greater than 26 ft/sec, suggesting that there the floor heaved upwards in the model. The test velocities, integrated from accelerometer time histories, show that not all the vertical velocities were removed during the critical impact phase, which is inconsistent with the photogrammetry.

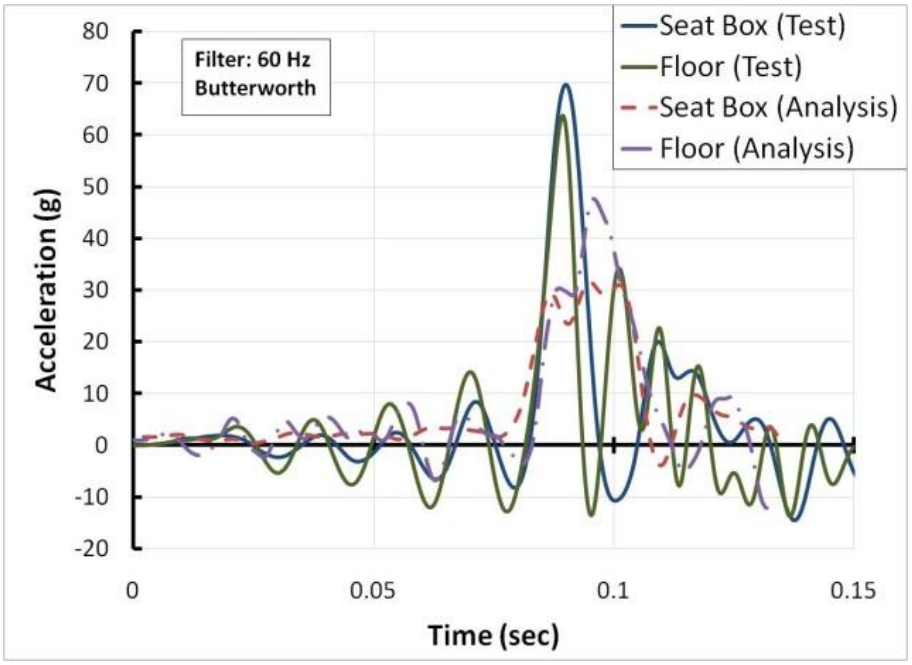

Figure 25. Comparison of test and analysis, pilot seat box and floor vertical acceleration; crash test without DEA.

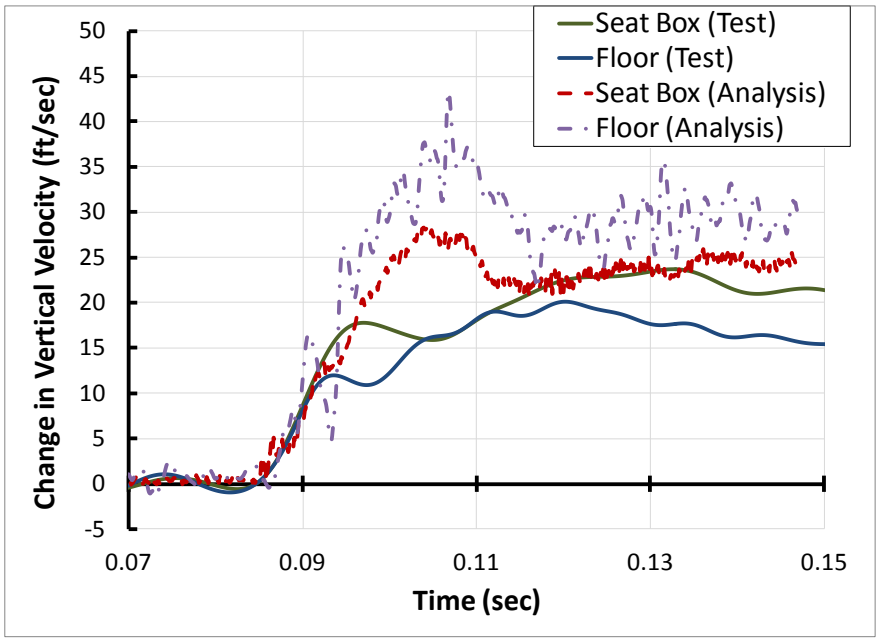

Figure 26. Comparison of test and analysis, pilot seat box and floor change in vertical velocity; crash test without DEA.

For simplicity, the shell thicknesses are considered constant over the whole region, which represents a smeared effective stiffness, whereas the actual hardware has edge doublers and rivets and small cutouts. These simplifying assumptions in the FEM may not account for multiple thin shell buckling and failure modes. This lack of model fidelity is further illustrated

when comparing the posttest pilot subfloor photographs to the analysis deformations in Figure 27. From the analysis, plastic deformation occurred along the shear panel, and no failure was seen of the keel beam. In contrast, posttest photographs indicate a substantial rippled region of the keel beam forward of the shear panel.

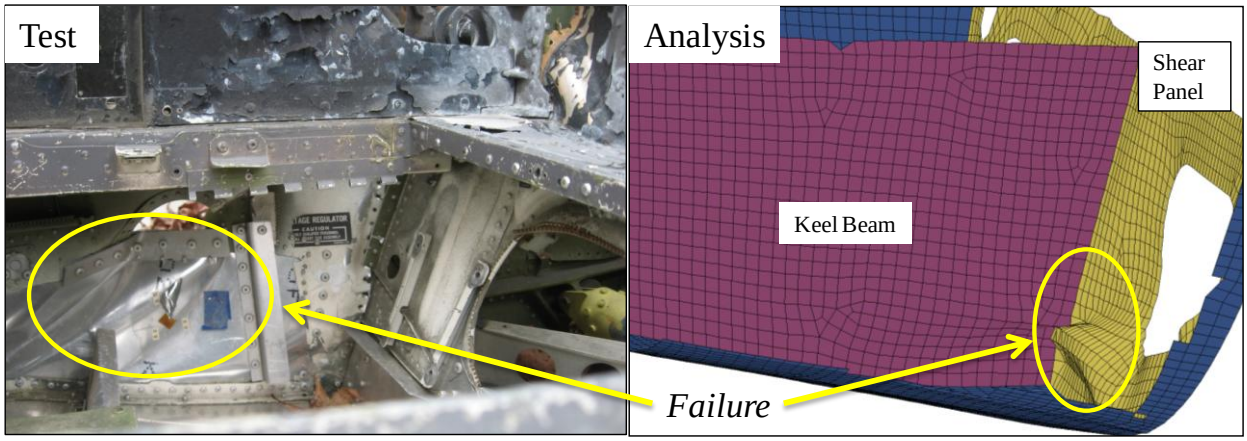

(a) Test. **(b) Analysis.**

Figure 27. Pilot subfloor: posttest photograph versus analysis.

The passenger floor accelerometer is mounted on a relatively stiff interface; thus, thin-walled effects are not introduced, and the filtered test data tracks better than the pilot response as shown with acceleration in Figure 28 and change in velocity in Figure 29. In this case, the passenger floor acceleration compares well in pulse shape and arrival time, but not in magnitude. Furthermore, the predicted pulse shape for the passenger floor is similar to the predicted pilot seat box and pilot floor pulse shapes.

Because the DEA significantly attenuated the impact response during the first crash test, one should not consider the model to be validated for more severe impact tests. The DEA acted as an isolator, imparting loads into the airframe while obscuring deficiencies in the airframe model. These deficiencies became apparent when severe loads produced highly nonlinear responses in the second full-scale test. There are multiple modes of failure in the test without the DEA, which may or may not need to be represented by the FEM. From the standpoint of matching acceleration pulse shapes, the FEM detail is adequate in the passenger region, but questionable for the pilot region. The previous assertion of an adequate FEM based on the crash test with the DEA was questioned. To determine if more physical detail is required in the model or if modifications to existing parameters is sufficient, a comprehensive model calibration was performed.

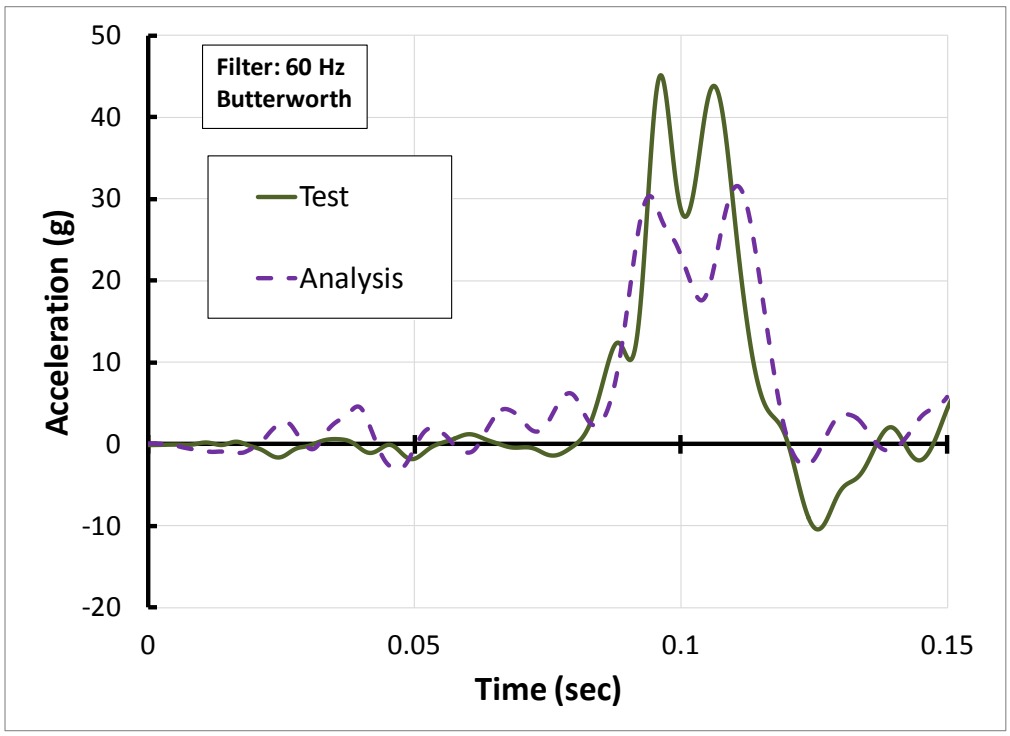

Figure 28. Comparison of test and analysis, passenger floor, vertical acceleration; crash test without DEA.

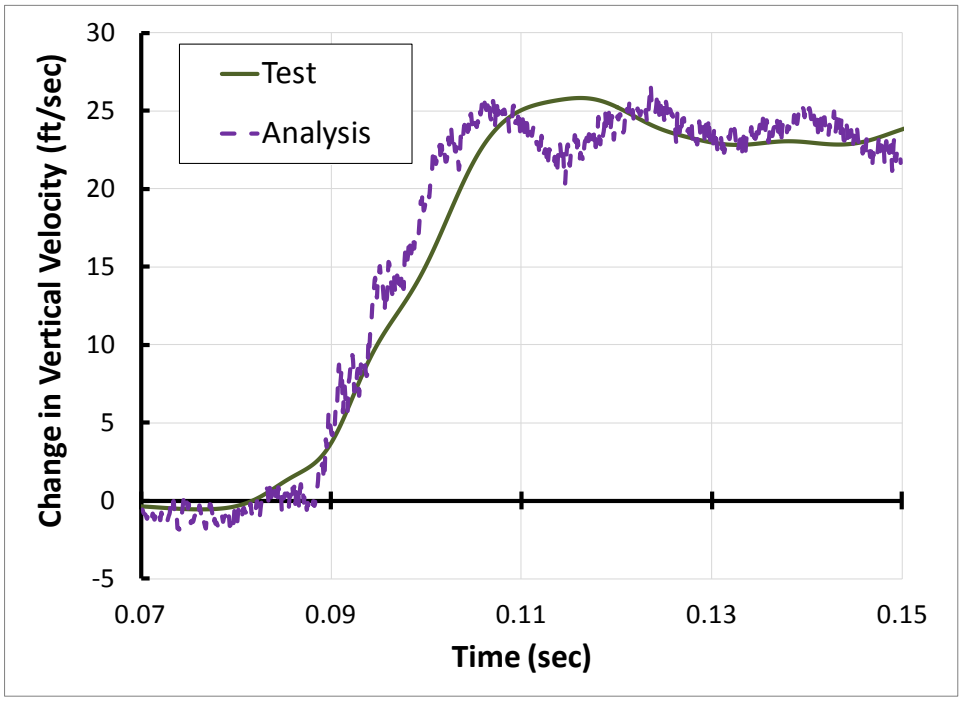

Figure 29. Comparison of test and analysis, passenger floor, change in vertical velocity; crash test without DEA.

AIRFRAME MODEL CALIBRATION BASED ON FULL-SCALE TEST WITHOUT DEA

Background

A more computationally rigorous formulation initially discussed in (ref. 16) is applied to results from the second test without the DEA to calibrate the FEM. Fundamental to the success of the model calibration effort is to establish if the model can predict the observed behavior in the presence of modeling uncertainty. Although there is no universally accepted metric to judge model adequacy, the approach used following the second test incorporates uncertainty propagation and quantification to assess model adequacy. From a baseline FEM, the first step in this approach is parameter selection (parameters being in this case material properties, structural dimensions, and initial conditions), which relies heavily on the analyst's knowledge and familiarity with the model and assumptions. After an initial parameter set is selected, uncertainty models to prescribe parameter variations are defined with the aid of empirical data, or, oftentimes, one must resort to engineering judgment. With an initial parameter set and an uncertainty model at hand, parameter importance is assessed using uncertainty propagation. Parameter values in this paper are created using the Halton (ref. 29) deterministic sampling technique. Time history results are processed to compute the metrics and to assess variability. A by-product of this step produces variance-based sensitivity results that are used to rank the parameters. In the end, adequacy of the parameter set is judged based on the probability of one being able to reconcile the test with the analysis.

Analysis of variance (ANOVA) is used for parameter sensitivity. In classical ANOVA studies, data are collected from multiple experiments while varying all parameters (factors) and also while varying one parameter at a time. These results are then used to quantify the output response variance due to variations of a particular parameter, as compared to the total output variance when varying all the parameters simultaneously. The ratio of these two variance contributions is a direct measure of the parameter importance. Sobol et al. (ref. 30) and others (ref. 31–33) have studied the problem as a means to obtain global sensitivity estimates using variance-based methods. To compute sensitivity using these variance based methods, one must be able to compute many response predictions as parameters are varied. For this report, after a suitable set of LS–DYNA solutions were obtained, response surface surrogates were used to estimate additional solutions.

The Extended Radial Basis Functions (ERBF) response surface method, as described by Mullur (ref. 34, 35), is used to estimate time histories and interpolate among LS–DYNA responses. In this adaptive response surface approach, the total number of response surface parameters computed equals $N(3n_p + 1)$, where n_p is the number of parameters and N is the number of LS–DYNA solutions. The user must also prescribe two additional parameters: 1) the order of a local polynomial (set to 2 in the present case), and 2) a smoothness parameter (set to 0.15 here).

Finally, the radial basis function is chosen to be an exponentially decaying function $e^{-(p-p_i)^2/2r_c^2}$ with characteristic radius r_c set to 0.15. A distinction with this response surface implementation is that ERBF is used to predict full time histories, as opposed to just extreme values. In addition, ERBF is able to match the responses with prediction errors of order 10^{-10} at the points used to create the surrogate.

Uncertainty propagation is conducted to evaluate uncertainty bounds and to gage the ability of the model to explain the observed behavior. The statistics of the 2-norm of a response vector between test and analysis are compared. An important benefit of using this metric is that it provides for a direct measure of multidimensional closeness of two models. In addition, when tracked as a function of time, closeness is quantified at each time step. Because parameters are uncertain, statistical measures of the metric need to be used to conduct assessments. With limited information about parameter uncertainty, a uniform distribution function is the most appropriate representation to model parameter uncertainty. This uncertainty model is used to create a family of *N* equally probable parameter vectors, where *N* is a scalar arbitrarily selected. From the perspective of a user, it is important to know the probability of being able to reconcile measured data with predictions, given a particular model for the structure and parameter uncertainty. To this end, let $Q(t,p) \triangleq \|v(t,p)\|_2$ be a scalar time varying function of the 2-norm of the system response vector *v*, using parameter vector *p* at time *t*. Furthermore, let $\underline{\sigma}(t) = \min_{\forall p} Q(t,p)$ be the minimum value over all parameter variations, and let $\overline{\sigma}(t) = \max_{\forall p} Q(t,p)$ be the maximum value. With these definitions and *N* LS–DYNA solutions, a calibration metric used to bound the probability of test values falling inside the analysis bounds is

$$M_1 = Prob\left[\underline{\sigma}(t) \le Q_e(t) \le \overline{\sigma}(t)\right] \gg \frac{1}{N} \tag{1}$$

where $Q_e(t)$ is the 2-norm of responses from the experiment. Note that *N* controls tightness of the bounds and also the number of LS–DYNA solutions required.

The use of norms, although convenient, tends to hide the spatial relationships that exist between responses at different locations in the model. In order to study this spatial multidimensional dependency explicitly, a different metric must be established. Work by Anderson et al. (ref. 36) and Horta et al. (ref. 37) proposed the application of singular value decomposition derived basis vectors or impact shapes. In this approach, time histories from analysis or experiments are decomposed as:

$$y(x,t) = \sum_{i=1}^{n} \sigma_i \phi_i(x) g_i(t) \tag{2}$$

In this form, the impact shape vector ϕ_i sized *m* x 1 contains the spatial distribution information for *m* sensors, *g*(t) contains the time modulation information, σ contains scalar values with shape participation factors, and *n* is the number of impact shapes to be included in the decomposition, often truncated based on allowable reconstruction error. Although eq. 2 is written in continuous time form, for most applications, time is sampled at fixed intervals such that $t = k\Delta T$ where the integer $k = 0,\ldots, L$ and ΔT is the sample time. In the discrete form of eq. 2, singular value decomposition is used to recover the basis functions (ϕ, σ, and g). The fractional contribution of the i^{th} impact shape to the total response is proportional to δ_i, defined as:

$$\delta_i = \frac{\sigma_i}{\sum_{l=1}^{n} \sigma_l} \tag{3}$$

Impact shapes can now be used to compare models using orthogonality. Orthogonality, computed as the dot product operation of vectors (or matrices), quantifies the projection of one vector onto another. If the projection is zero, vectors are orthogonal, i.e., distinct. This same idea applies when comparing test and analysis impact shapes. Numerically, the orthogonality metric is computed as:

$$M_2 = \breve{\Phi}^T \breve{\Psi} \tag{4}$$

where $\breve{\Phi}$ is sized *m* x *l* with *l* measured impact shapes at *m* locations and $\breve{\Psi}$ sized *m* x *l* are shapes computed using simulation data. Note that both $\breve{\Phi}$ and $\breve{\Psi}$ are normalized matrices such that $\breve{\Phi}^T\breve{\Phi} = I$ and $\breve{\Psi}^T\breve{\Psi} = I$. Because individual impact shape vectors are stacked column-wise, metric M_2 is a matrix sized *l* x *l* with diagonal values corresponding to the vector projection numerical value. If vectors are identical then their projection equals 1. Consequently, when evaluating models, multidimensional closeness with the experiment is judged based on similarity of impact shapes and shape contributions.

If the model can be reconciled based on both time and spatial calibration metrics, a parameter set is computed that minimizes the squared sum of the prediction error, as defined in eq. 5. The matrix *W* is used to scale or remove data points from the time history.

$$J = \sum_{k=1}^{L-1} (y(k\Delta T) - y_e(k\Delta T))^T W (y(k\Delta T) - y_e(k\Delta T)) \tag{5}$$

Optimization is based on the constrained optimization using response surface (CORS) scheme developed by Regis and Shoemaker (ref. 38). Specifically, the algorithm starts by looking for parameter values away from the *N* initial set of LS–DYNA solutions, then slowly steps closer to known solutions by solving a series of local constrained optimization problems. This optimization process will produce a global optimum if enough steps are taken. Of course, the user controls the number of steps and therefore the accuracy and computational expense in conducting the optimization. In cases where the predictive capability of the surrogate model is poor, CORS adds solutions in needed areas. Because parameter uncertainty is not used explicitly in the optimization, this approach is deterministic. If a probabilistic approach was used instead, in addition to a reconciling set, the user should also be able to determine the probability that the parameter set found is correct. These metrics will now be used to analyze the data from the second test without the DEA.

Calibration Results

For the purposes of this calibration effort, 19 sensor locations, containing either triaxial or uniaxial accelerometers and totaling 23 channels, were used. At the outset of performing calibration runs, the velocity 2-norm of the sensor set was used as a comparison metric. Velocity metrics were used because high frequency responses of structures evident in acceleration time histories become naturally filtered once integrated to velocity. Direct comparison between test and analysis velocities is only achievable by integrating the test accelerometer time histories. The integrated test curves are shifted to match to the local initial velocities that are directly output in the respective local coordinate systems from the analysis. For many of the accelerometers, integration of the signal revealed drifting and inconsistent changes in velocity. The contribution

of drift was unique from sensor to sensor and was difficult to detrend. The accelerometers in the calibration sensor set could be successfully integrated and, therefore, retained.

Altogether, seven different calibration cycles were performed with different parameter sets and varying ranges for each parameter. For the first several calibration cycles, initial conditions were chosen as parameters to vary based on the supposition that there was variability in the initial velocities and attitudes from photogrammetry. However, impact conditions such as vertical and horizontal velocities and pitch angle had the highest contribution to the total response variance, which tended to overshadow the importance of structural parameter values. The photogrammetry results were reexamined, and initial conditions permanently fixed.

As calibration cycles were performed, it was also evident that solely using velocity as the comparison metric had a disadvantage. Integration removes critical low- to mid-frequency modes and responses that could be important in identifying shifting load paths as the airframe plastically deforms. Both acceleration and velocity 2-norms were used to determine whether the parameter sets and their range of values were appropriately chosen.

Because of runtime stability issues, the ATD FEMs were removed from the model and their masses evenly distributed onto the seat frames and floor. In the meantime, the ATD FEM model was calibrated independent of the airframe calibration based on results from drop tests of the ATD onto a rigid seat platform (ref. 17). Figure 30a shows the FEM representation used for calibration, and Figure 30b shows the calibration sensor locations.

(a) Calibration model.

Figure 30. Calibration FEM.

(c) Calibration sensor locations.

Figure 30. Concluded.

Parameter selection for the calibration study addresses two essential aspects of the model, stiffness and plasticity. Most of the critical airframe components in the load path are modeled with shell elements with effective stiffness properties. Seemingly, the thickness of components could be directly measured from the test article. However, the presence of rivets, doublers, and small stiffeners that could not be included in the model without sacrificing computational efficiency would stiffen the test article. Conversely, cutouts and holes would reduce the stiffness. The term "effective" accounts for the omission of these features. To change the effective in-plane and bending stiffness, either the modulus of elasticity or the thickness defined in the shell property can be modified. For this study, the thickness was modified for four structural components: belly thickness, keel beam thickness, seat box thickness, and seat box bulkhead thickness. These parameters were identified to significantly influence the load path and impact response. Additionally, because the airframe is a combination of different alloys of thin sheet or cast aluminum, the fifth parameter selected was the initial yield stress. Yield stress was chosen specifically for parts in the floor and subfloor region where extensive damage occurs and addresses the plasticity of the aluminum components.

To illustrate the value of computing the calibration metric M_1, the acceleration and velocity 2-norms are plotted in Figure 31 for a set of 60 LS–DYNA runs while varying the five parameters shown in the table in Figure 31. All acceleration data is low-pass filtered to SAE CFC 60. At this point the user must determine if the analysis 2-norm bounds, created with 60 LS–DYNA runs, envelop the test bounds. Based on the number of runs, the probability of being able to reconcile the model with the test if the experiment is outside the bounds is much less than 1/60. From Figure 31 it is apparent that both acceleration and velocity 2-norm bounds have regions of the

response that fall outside the analytical bounds. Hence, the LS–DYNA model is not likely to reconcile with the test in its present form.

Additional acceleration results revealed that the time and spatial variation of load transfer are not matched. At the point of belly impact, there are large accelerations in the pilot and copilot region that contribute highly to the 2-norm. Qualitatively, the amount of deformation witnessed from posttest inspection of the subfloor is lower than the analytical predictions. To prevent early yielding and redistribution of loads, the range of probable keel beam thicknesses needed to be increased. This finding was also confirmed from the variance analysis shown in Figure 32. In here, the contribution of a single parameter variance to the total variance was computed to determine if parameters affected the response or not. In Figure 32, the sum total for the variance contribution of each parameter approaches one. From Figure 32, the parameter with the highest variance contribution immediately following belly impact (in red) is the keel beam thickness.

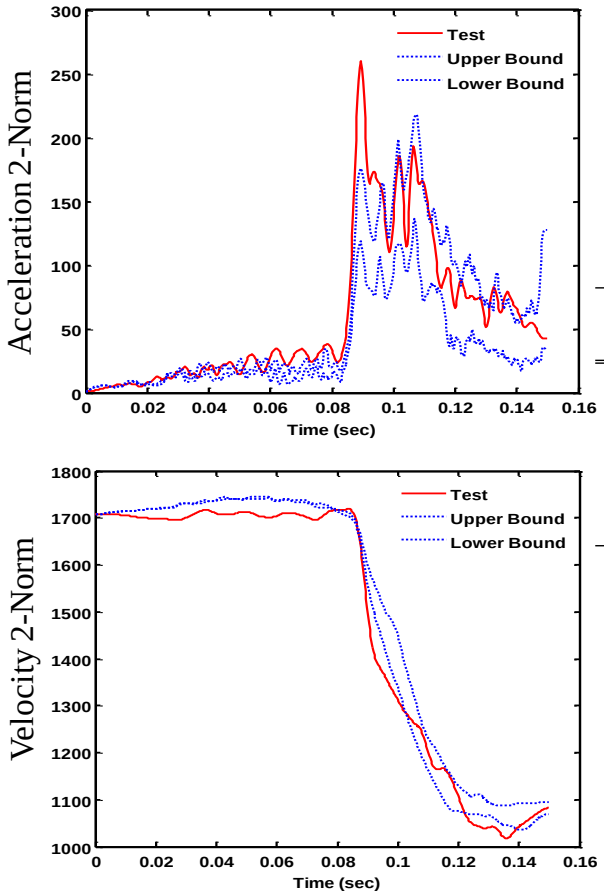

No.	Parameter Description	Nominal	Upper Bound	Lower Bound
1	belly thickness (in)	0.09	0.12	0.08
2	keel beam thickness (in)	0.04	0.07	0.03
3	seat box thickness (in)	0.1	0.12	0.08
4	seat box bulkhead thickness (in)	0.05	0.07	0.03
5	Yield Stress (psi)	40,000	45,000	35,000

Figure 31. Uncertainty bounds for interim calibration cycle.

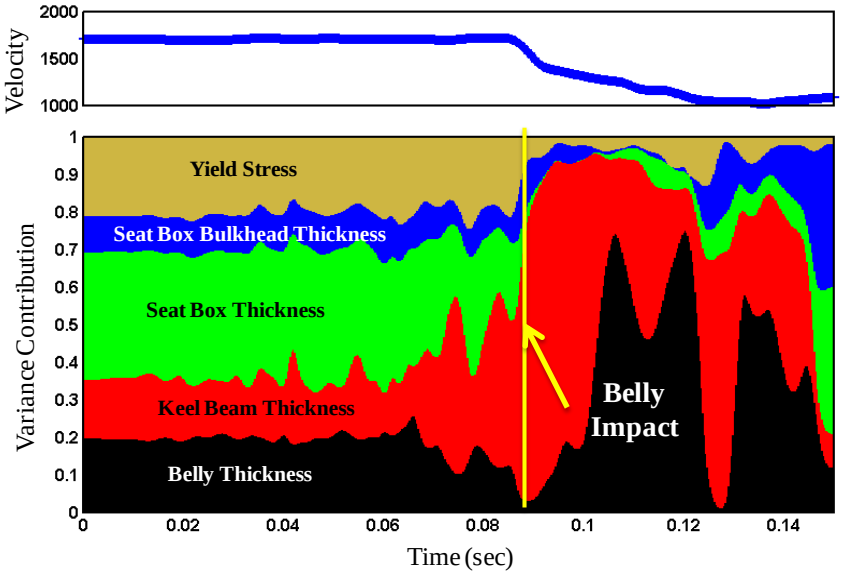

Figure 32. Variance for interim calibration cycle.

Calibration runs were conducted with the keel beam thickness increased to a range of 0.10 to 0.15 inches. A total of 60 LS–DYNA runs were performed using the newly defined keel beam parameter range, combined with four other parameters previously defined. Uncertainty bound results for acceleration indicate that the increase in keel beam thickness has shifted the peak acceleration response to align better with the test results. Results in Figure 33 indicate that, based on acceleration and velocity 2-norm, it is more likely that a set of parameters within the range established could reconcile the model with the test.

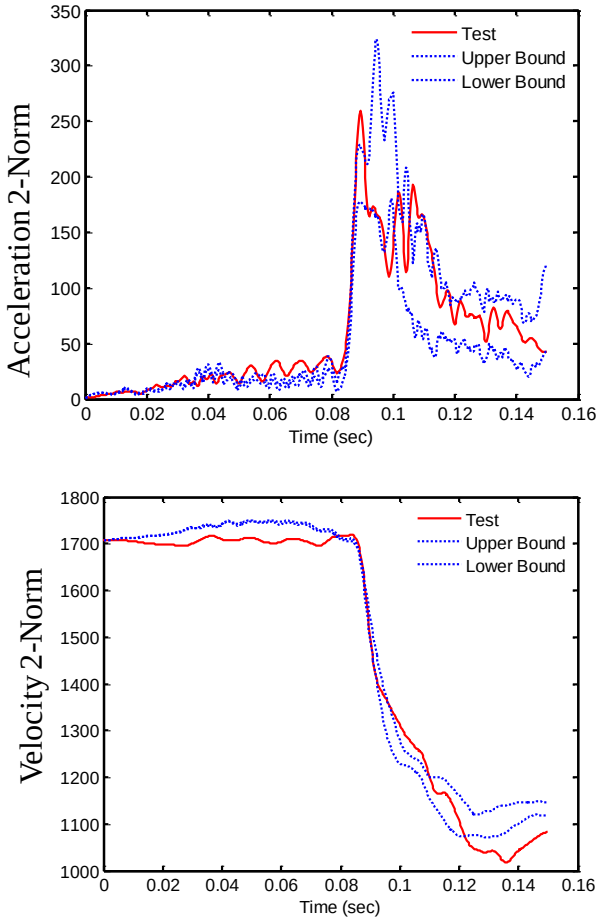

No.	Parameter Description	Nominal	Upper Bound	Lower Bound
1	belly thickness (in)	0.09	0.12	0.08
2	keel beam thickness (in)	0.12	0.15	0.10
3	seat box thickness (in)	0.1	0.12	0.08
4	seat box bulkhead thickness (in)	0.05	0.07	0.03
5	Yield Stress (psi)	40000	45000	35000

Figure 33. Uncertainty bounds for final calibration cycle.

The spatially based metric M_2 was used to perform orthogonality checks between the test and analysis basis vectors. Orthogonality results for the baseline set of parameters and parameters for Run #44 (of 60 runs), which is similar to the baseline but has a yield stress nearing the lower bound and a seat box thickness nearing the upper bound, are shown in Figure 34. The size of the orthogonality table is equal to the number of impact shapes chosen for both test and analysis, in this case n = 10. Basis vectors generated from acceleration time histories are compared for test and analysis; good agreement is indicated by the black and dark blue colors. The parameter set of Run #44 shows improved orthogonality for impact shapes 5 and 6. This does not imply that the selected case is optimal, but it does indicate that a slight change in these parameters can significantly alter the impact shapes. Because of time constraints and the fact that, with a model this complex, more component data was required, no additional calibration cycles were attempted. During this calibration phase, many problem areas of the model surfaced, but without additional data, they are difficult to correct.

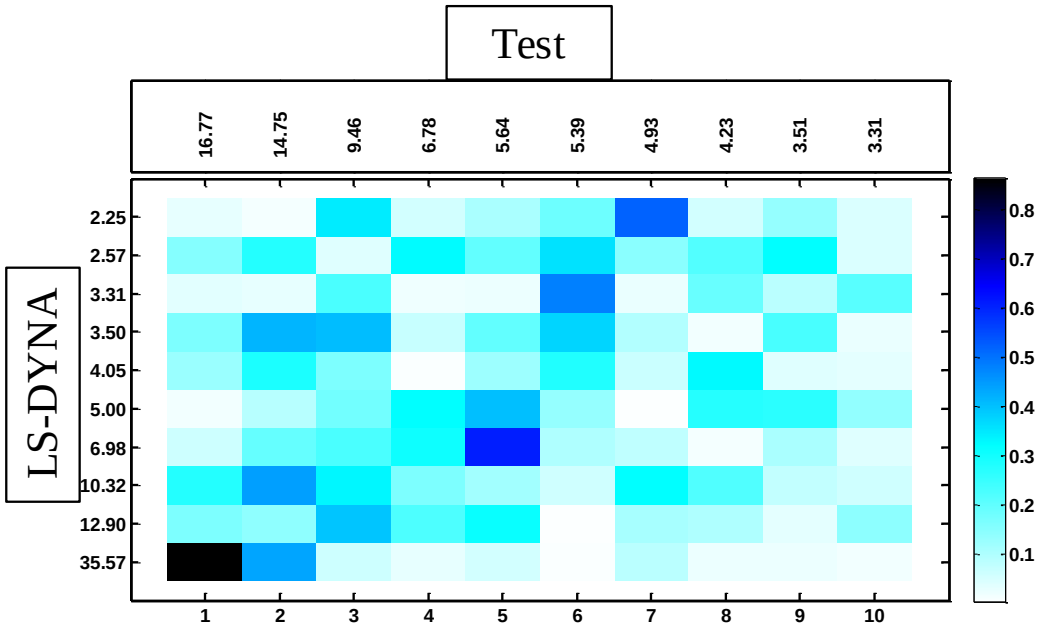

(a) Baseline.

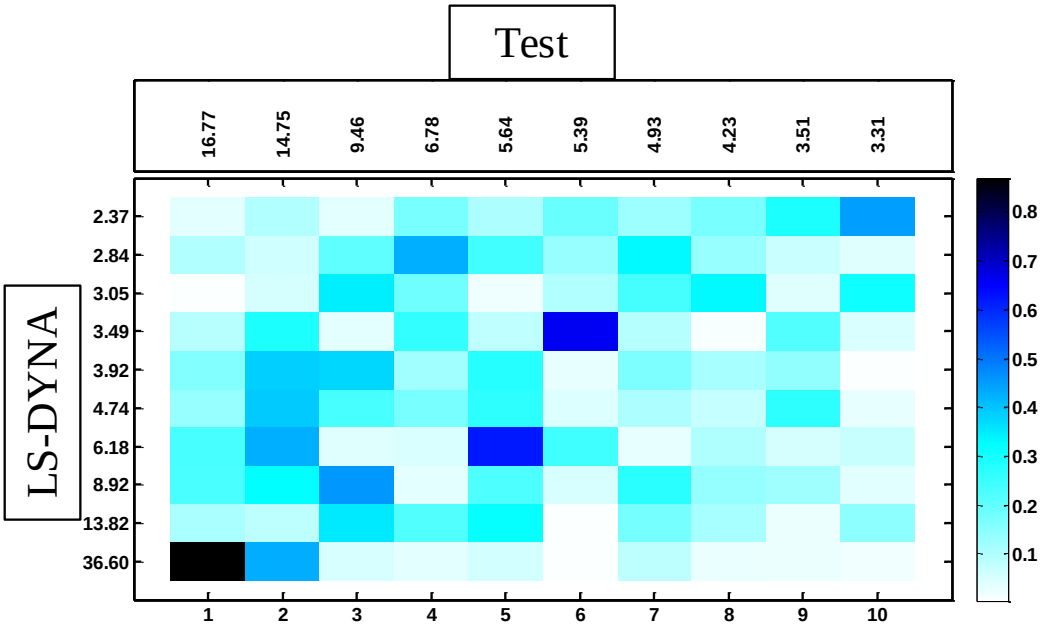

(b) Run #44.

Figure 34. Orthogonality for final calibration cycle.

UPDATED RESPONSES FOR CALIBRATED SYSTEM-INTEGRATED MODEL

Crash Test without DEA

The updated LSTC Hybrid III ATD FEM was calibrated using data from vertical drop tests (ref. 17). The first modification performed was mesh refinement. With mesh refinement, the overall contact stiffness on the ATD was improved, and the noise present in the original vertical acceleration time histories was eliminated. In the original ATD model, several rigid parts in contact with the seat platform caused peak acceleration readings to rise above reasonable values. For this reason, the thighs, kneecaps, and feet in the ATD model were recharacterized using deformable material models. A layer of rubber shell elements was overwrapped onto the pelvis and upper thigh parts to represent the skin of the ATD. To represent the abdominal insert and to restrict flailing of the ATD upon impact, linear springs were inserted between the ribcage and the pelvic insert. The spring stiffness was based on the effective material properties of the abdominal insert. Restraints were not incorporated back into the fully calibrated FEM because it was evident from test results that restraints were not significantly loaded during the initial impact and rebound. Restraints only became loaded during torso flail, which occurred well beyond the time duration considered here.

The fully calibrated MD-500 FEM with the updated ATD FEMs is shown in Figure 35 and consisted of approximately 590,000 elements in total. The calibrated set of values for the airframe FEM without the DEA is shown in Table 2. Of the five parameters, three remained close to the nominal value (belly thickness, keel beam thickness, and seat box thickness), while the seat box bulkhead thickness approached the upper bound, and the yield stress approached the lower bound. These changes are similar to the parameter change in Run #44.

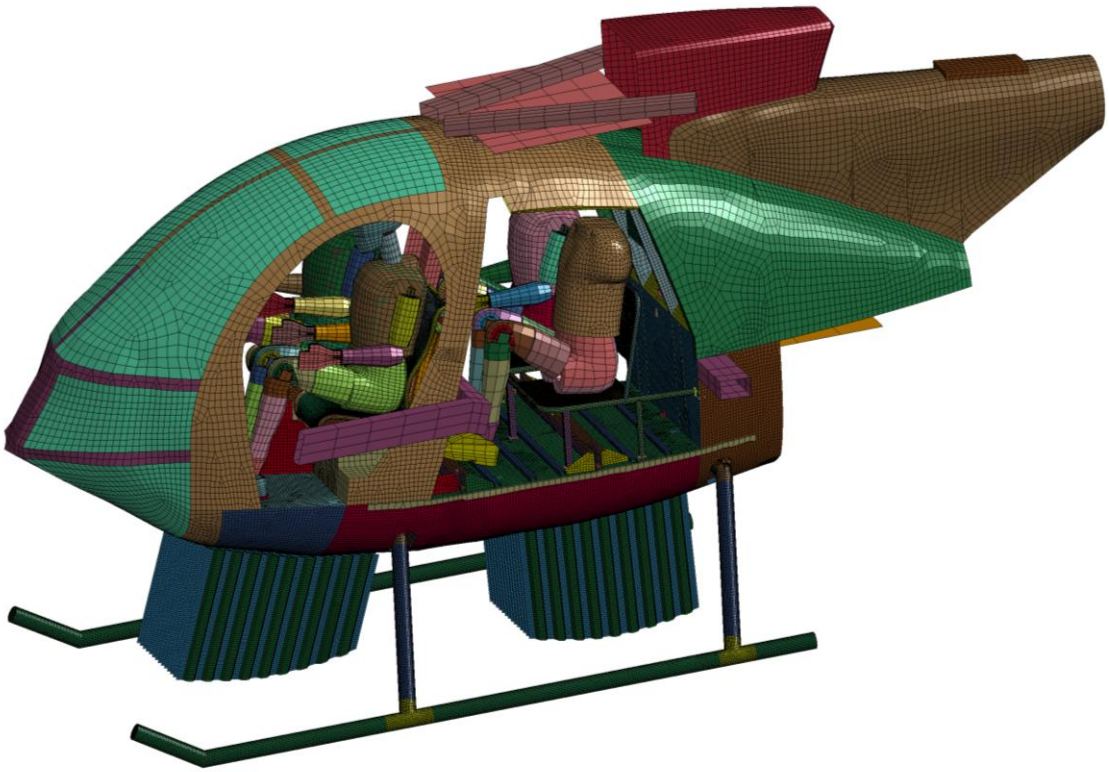

Figure 35. Final calibrated system-integrated FEM.

Table 2. Calibrated parameters.

No.	Parameter Description	Nominal	Upper Bound	Lower Bound	Calibrated
1	belly thickness (in)	0.09	0.12	0.08	0.089
2	keel beam thickness (in)	0.12	0.15	0.10	0.12
3	seat box thickness (in)	0.10	0.12	0.08	0.11
4	seat box bulkhead thickness (in)	0.05	0.07	0.03	0.065
5	Yield Stress (psi)	40,000	45,000	35,000	35,210

The original approach of investigating individual acceleration time histories for calibration and validation had been set aside in favor of the uncertainty estimation, parameter sensitivity, and impact shape orthogonality approach. Nonetheless, it is worthwhile to revisit the time histories after modifying the model. The shape, duration, and magnitude of acceleration time histories remain important indicators when determining input pulses for seat certification or when evaluating occupant injury criteria such as Eiband, Dynamic Response Index, and Brinkley Index.

The vertical acceleration at the pilot floor is plotted in Figure 36. The overall pulse duration remains about 0.050 seconds. Note that the calibrated model shows a higher acceleration peak magnitude (60 g) than the original model (47 g) and better matches the test peak magnitude better (63 g).

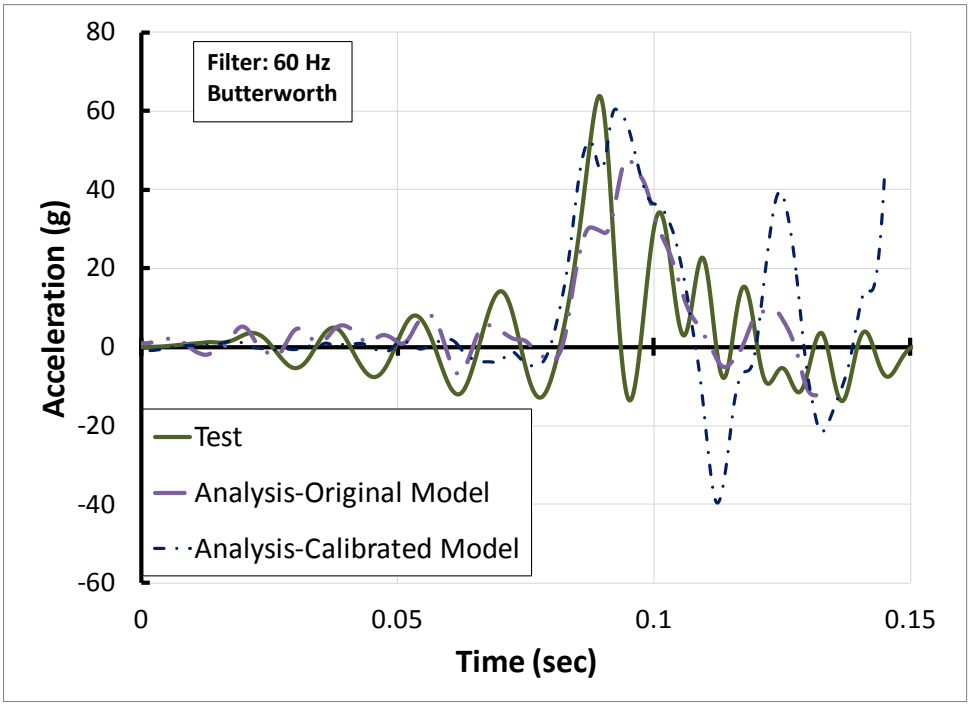

Figure 36. Pilot floor vertical acceleration; crash test without DEA.

On the other hand, the passenger floor vertical accelerations are plotted in Figure 37. Although the analytical waveform shapes and duration agree well with the test, the peak magnitude of the original model was less than the test acceleration by 15 g. Thus, the increase in keel beam stiffness has caused an overcorrection in peak magnitude, from 30 g to 70 g. By treating the keel beam as one continuous property, the pilot–copilot region was calibrated properly, but the model behaves too conservatively when examining the passenger region. Hence, during calibration, the keel beam area should have been split into separate segments to adjust the areas independently.

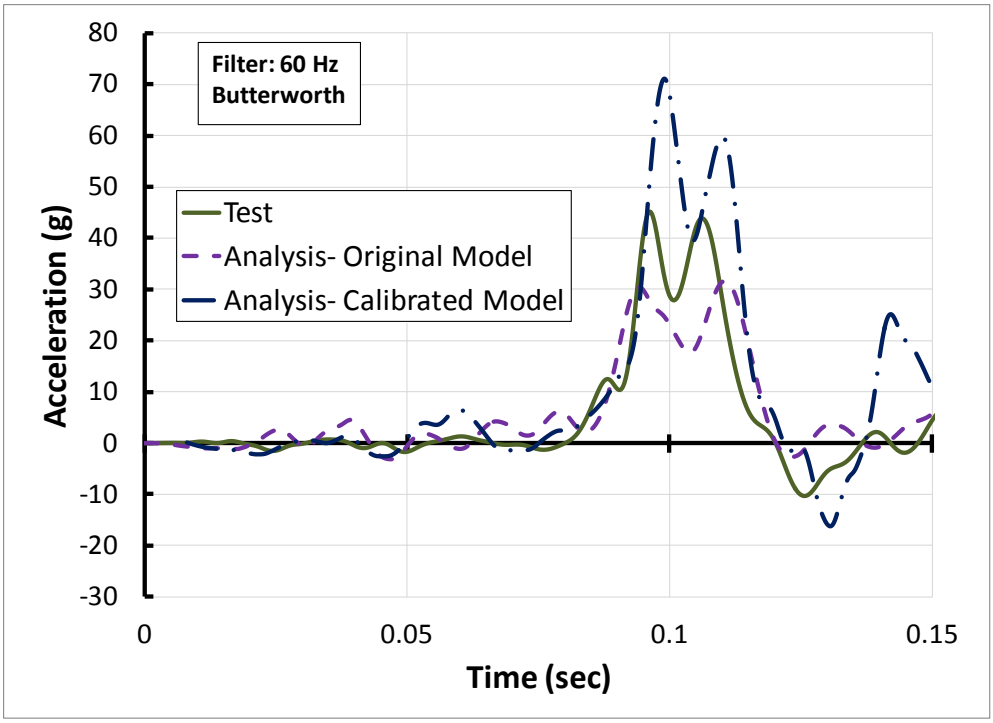

Figure 37. Passenger floor vertical acceleration; crash test without DEA.

Figure 38 shows results for the vertical acceleration of the pilot pelvic area. To contrast, the original model shows a very high pelvic acceleration (140 g), while the calibrated model acceleration was reduced to 100 g. Despite all of the improvements within the ATD FEM, the analysis magnitude exceeds the test magnitude (42 g) by over a factor of two. For both the original and calibrated model, the acceleration spikes could be attributed to the pelvis and seat mesh contacting the seat pan. During posttest inspection, damage was plainly visible on the seat pan, suggesting that contact occurred. However, the spike in load is only evident in the analysis. More modifications are required in the LSTC ATD FEM, including further conversion of rigid components to deformable for instance, if results are to be reliably used to evaluate occupant injury.

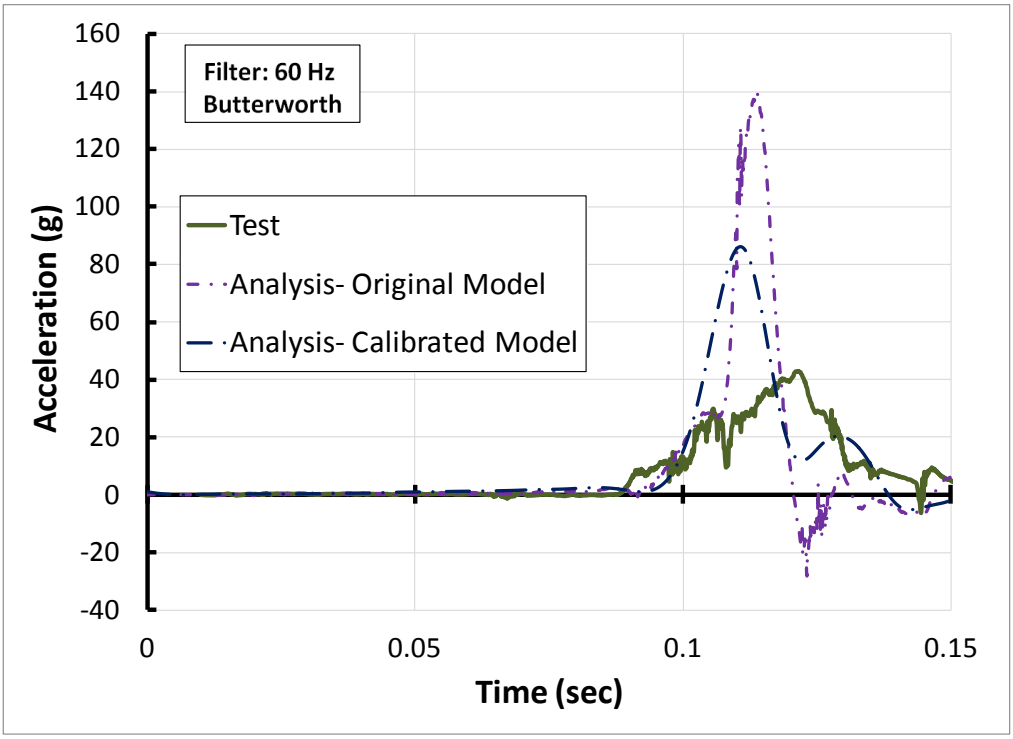

Figure 38. Pilot pelvic vertical acceleration; crash test without DEA.

Crash Test with DEA

The pilot seat vertical accelerations are plotted in Figure 39. The responses for the original and calibrated model are similar in shape and magnitude, with load limiting crush performance of the DEA near 10 g. However, the calibrated model does capture the abrupt rise in acceleration at the end of the pulse. This behavior was not seen with the original model. The stiffening of the subfloor, specifically the keel beam, allowed the compaction phase of the DEA crushing to be transmitted into the cockpit. Similarly, the passenger floor vertical accelerations in Figure 40 also reveal a rise in loads near the end of the pulse.

As shown in Figure 41, the calibrated ATD shows improvements in pelvic vertical acceleration predictions, not unlike the ATD results for the crash test without DEA. The pulse shape is more flattened and loads are reduced from 25 g to 18 g. Nevertheless, the differences are still significant, and the accuracy of the ATD model is still questionable.

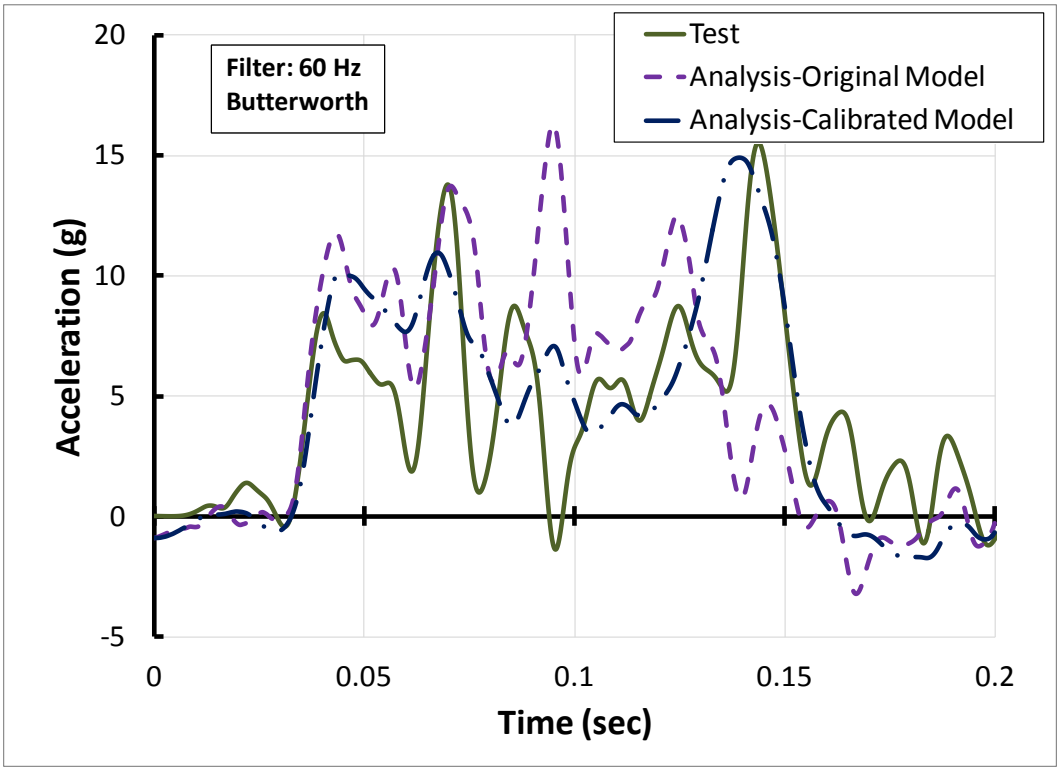

Figure 39. Pilot floor vertical acceleration; crash test with DEA.

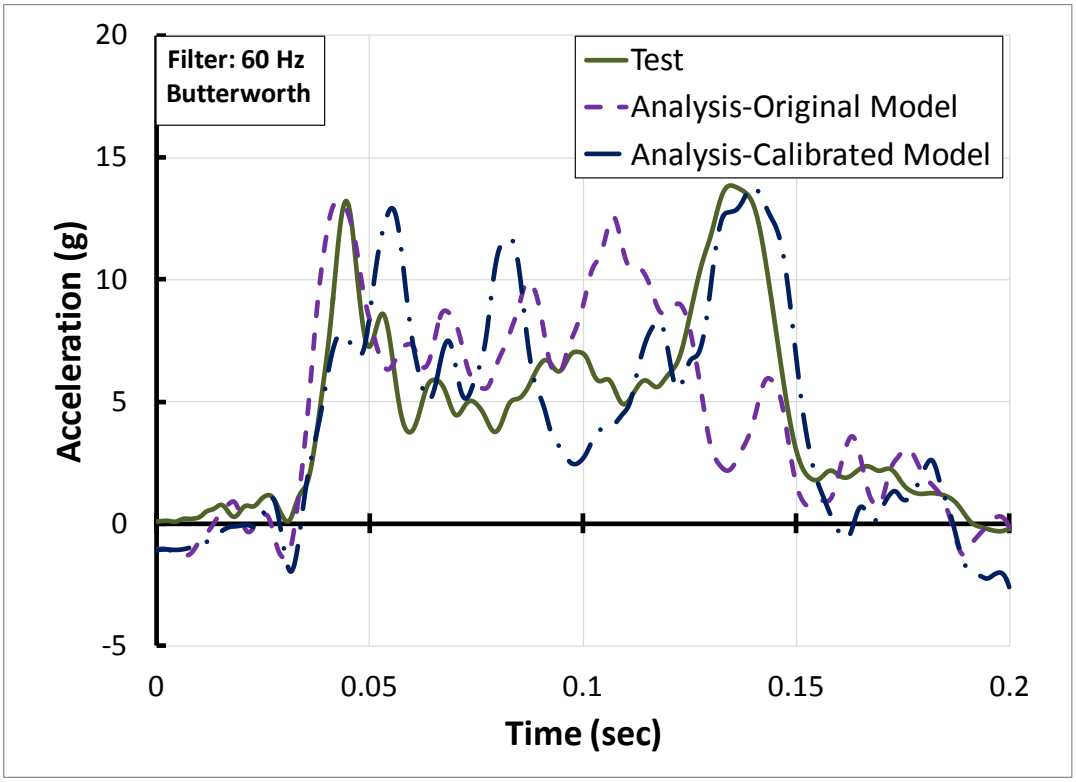

Figure 40. Passenger floor vertical acceleration; crash test with DEA.

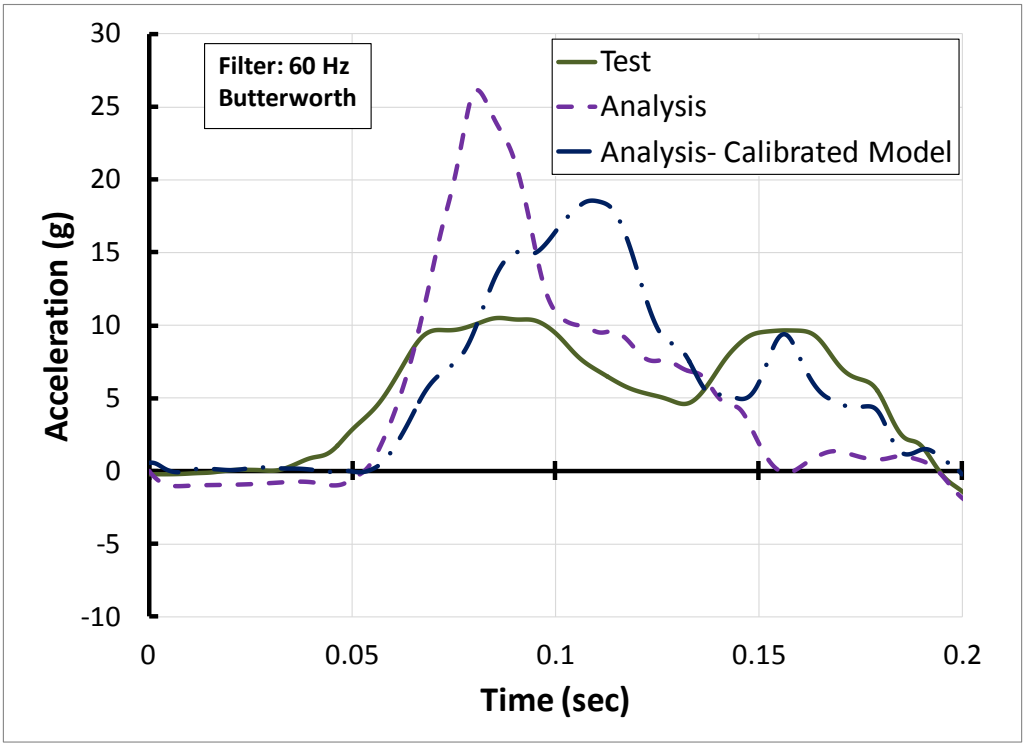

Figure 41. Pilot pelvic vertical acceleration; crash test with DEA.

CONCLUDING REMARKS

Two full-scale helicopter crash tests, sponsored by the NASA Subsonic Rotary Wing Program, were conducted in an effort to evaluate new structural concepts to improve rotorcraft crashworthiness and to increase occupant survivability. In the first test a helicopter was fitted with a Deployable Energy Absorber (DEA) system, and the second test was conducted without the DEA. The tests demonstrated a peak acceleration reduction upon impact by a factor of three when using the DEA.

A system-integrated finite element model for simulating rotorcraft crashworthiness was developed and correlated to the tests. Component level analyses and tests were conducted to establish the material properties of the DEA, the crush tube shock struts, and the seat mesh. Full-scale mass simulator tests were conducted to develop confidence in both analysis and test methodologies and to reduce risk. Good agreement for skid gear strains and center of gravity accelerations was seen between the test and the analysis.

Acceleration time histories at the pilot and passenger floor were compared to analysis for both crash tests. Agreement in acceleration magnitudes and pulse duration was seen between the test and the analysis for the crash test performed with the DEA. The acceleration waveforms and peak values were significantly different between the test and the analysis for the crash test performed without the DEA. One reason for this discrepancy is the fact that acceleration levels for the test with the DEA were significantly lower and, therefore, less energy went into deforming the fuselage. Consequently, model fidelity played less of a factor for the test with the DEA.

LS–DYNA model calibration was performed based on two new calibration metrics: (1) a 2-norm velocity bound metric, and (2) orthogonality of test and analysis impact shapes. Results with metric 1 were used to assess the probability of reconciling the test with the analysis after uncertainty propagation studies. Calibration parameters were selected or removed based on the results of metric 1. Orthogonality plots were used to determine if certain parameter sets produced better spatial agreement and clarified stiffness disparities for critical components. Results from this effort highlighted model deficiencies that were unexplainable without additional component data.

The FEM of the airframe was validated by comparing acceleration time histories for the pilot and passenger regions following calibration. One key outcome of the calibration was the stiffening of the subfloor, particularly along the keel beam. Waveforms magnitudes and shapes were improved from the baseline models and relative error was reduced for both crash tests. The FEM of the ATD used in this study is not valid when computing internal forces such as pelvic acceleration and lumbar load, and improvements in the LSTC FEM detail are necessary.

Several lessons learned from this effort should be considered in the future when conducting tests for the purpose of calibrating analytical models. First, the sensor suite must cover all critical components and should be mounted on relatively stiff components to avoid high frequency saturation of the acceleration output. Second, the accelerometers should be calibrated to ensure their velocity integration is accurate. Third, multiple validation metrics should be applied between the test and the analysis, which comprehensively identify modeling deficiencies,

evaluate parameter importance, and propose required model changes. Finally, when dealing with very complex structures, a building block approach to model calibration will help break up the problem into more manageable subsystems. The objective of certification by analysis cannot be achieved practically without methodologies established similar to those discussed here.

REFERENCES

1. Jackson, K., Kellas, S, Horta, L. G., Annett, M. S., Polanco, M. A., Littell, J. D., and Fasanella, E. L., "Experimental and Analytical Evaluation of a Composite Honeycomb Deployable Energy Absorber," NASA/TM–2011–217301, November 2011.

2. Anonymous, Military Standard, MIL–STD–1290A (AV), Light Fixed- and Rotary-Wing Aircraft Crash Resistance, Department of Defense, Washington DC, 20301, 26 September 1988.

3. Code of Federal Regulations, Federal Aviation Regulations for Aviation Maintenance Technicians FAR AMT, Part 27 Airworthiness Standard: Normal Category Rotorcraft, 27.562 Emergency Landing Dynamics.

4. Bolukbasi, A., Crocco J., Clarke, C., Fasanella, E., Jackson, K., Leary, P., Labun, L., Mapes, P., McEntire J., Pelletiere, J., Pilati, B., Rumph, F., Schuck, J., Schultz, M., Smith, M., and Vasquez, D., "Full Spectrum Crashworthiness Criteria for Rotorcraft," RDECOM TR 12–D–12, December 2011.

5. Khalil, T. B. and Sheh, M. Y., "Vehicle Crashworthiness and Occupant Protection in Frontal Impact by FE Analysis–An Integrated Approach," Proceedings of Crashworthiness of Transportation Systems: Impact and Occupant Protection, Kluwer Academic Publisher, 1997, pp. 363–399.

6. Kan, C. D., Marzougui, D., Bahouth, G. T., and Bedewi, N. E., "Crashworthiness Evaluation using Integrated Vehicle and Occupant Finite Element Models," *International Journal of Crashworthiness*, Vol. 6, No. 3, 2001, pp. 387–397.

7. Wittlin, G. and Gamon, M. A., "Experimentally Verified Analytical Techniques for Predicting Vehicle Crash Responses," Proceedings of the AIAA 11th Annual Meeting and Technical Display, AIAA Paper No. 75–273, February 1975.

8. Cronkhite, J. D., and Mazza, L. T.: "KRASH Analysis Correlation with the Bell ACAP Full-Scale Aircraft Crash Test," Proceedings of the National Technical Specialists' Meeting on Advanced Rotorcraft Structures: Requirements vs. Opportunities, a Look at the Future, VA, October 1988.

9. Jackson, K. E., Fasanella, E. L., and Boitnott, R. L., "Full-Scale Crash Test and Finite Element Simulation of a Composite Prototype Helicopter," NASA/TP–2003–212641, 2003.

10. Wittlin, G., Smith, M., and Richards, M., "'Airframe Water Impact Analysis Using a Combine MSC/DYTRAN-DRI/KRASH Approach," Proceedings of the American Helicopter Society 53rd Annual Forum, Virginia Beach, CA, 29 April–1 May 1997.

11. Hallquist, John Q., "LS–DYNA Keyword User's Manual," Version 971, Revision 5.0, Livermore Software Technology Company, Livermore, CA, May 2010.

12. Jackson, K. E., and Fasanella, E. L., "Crash Simulation of a Vertical Drop Test of a Commuter-Class Aircraft," *International Journal of Crashworthiness*, 1754–2111, Vol. 10, No. 2, 2005, pp. 173–182.

13. NASA–STD–7009, "Standards for Models and Simulations," 11 July 2008.

14. Sprague, M. A. and Geers, T. L., "Spectral Elements and Field Separation for an Acoustic Fluid Subject to Cavitation," *Journal of Computational Physics*, Vol. 162, 2003, pp. 184–149.

15. Russell, D. M., "Error Measures for Comparing Transient Data: Part I: Development of a Comprehensive Error Measure," Proceedings of the 68th Shock and Vibration Symposium, 2006, pp. 175–184.

16. Horta, L. G., Reaves, M. C., Annett, M. S., and Jackson, K. E., "Multi-Dimensional Calibration of Impact Dynamic Models," Proceedings of the IMAC-XXIX Conference and Exposition on Structural Dynamics, Jacksonville, FL, 31 January–3 February 2011.

17. Polanco, M., and Littell, J. D., " Vertical Drop Testing and Simulation of Anthropomorphic Test Devices," 67th AHS Forum, Virginia Beach, VA, 3–5 May 2011.

18. Littell, J. D., "A Comparative Analysis of Two Full Scale MD-500 Helicopter Crash Tests," Proceedings of the 2010 SEM Annual Conference & Exposition on Experimental and Applied Mechanics, Uncasville, CT, June 2011.

19. Roberts, J., Merkle, A., Biermann, P., Ward, E., Carkhuff, B., Cain, R., and O'Connor, J., "Computational and Experimental Models of the Human Torso for Non-Penetrating Ballistic Impact," *Journal of Biomechanics*, Vol. 40, No. 1, 2007, pp. 125–136.

20. Kellas, S., "Deployable Rigid System for Crash Energy Management," U.S. Patent Nos. 6,755,453 on 29 June 2004; 6,976,729 on 20 December 2005; and 7,040,658 on 9 May 2006.

21. Littell, J., "Large Field Photogrammetry Techniques in Aircraft and Spacecraft Impact Testing," SEM Annual Conference & Exposition on Experimental and Applied Mechanics, Indianapolis IN, June 2010.

22. Polanco, M., "A Parametric Study on a Shell-Based Model of a Kevlar/Epoxy Composite Honeycomb," AHS Technical Specialists Meeting on Rotorcraft Structures and Survivability, Williamsburg, VA, 27–29 October 2009

23. Anonymous, Structural Repair Manual, CSP–SRM–6, MD Helicopters, Inc, Mesa, AZ, May 2006.

24. Guha, S., Bhalsod, D., and Krebs, J., "LSTC Hybrid III Dummies, Positioning & Post-Processing, Dummy Version: LSTC.H3.103008_v1.0," LSTC Michigan, 30 October 2008.

25. Tabiei, A., Lawrence, C., and Fasanella, E., "Validation of Finite Element Crash Test Dummy Models for Predicting Orion Crew Member Injuries During a Simulated Vehicle Landing," NASA/TM–2009–215476, 2009.

26. Eiband, M. A., "Human Tolerance to Rapidly Applied Accelerations: A Summary of the Literature," NASA Memorandum 5–19–59E, June 1959.

27. Brinkley, J. W. and Shaffer, J. T., "Dynamic Simulation Tecniques for the Design of Escape Systems: Current Applications and Future Air Force Requirements," Symposium on Biodynamic Models and their Applications, AMRL–TR–71–29, Wright-Patterson Air Force Base, Dayton, OH, Aerospace Medical Research Laboratory, 1970.

28. Brinkley, J. W., Specker, L. J., and Mosher, S. E., "Development of Acceleration Exposure Limits for Advanced Escape Systems," NATO AGARD Proceedings, AGARD–CP–472, 1990.

29. Halton, J. H., "On the Efficiency of Certain Quasi-Random Sequences of Points in Evaluating Multi-Dimensional Integrals," *Numerische Mathematik*, Vol. 2, 1960, pp. 84–90.

30. Sobol, I. M., Tarantola, S., Gatelli, D., Kucherenko, S. S, and Mauntz, W., "Estimating Approximation Error When Fixing Unessential Factors in Global Sensitivity Analysis," *Reliability Engineering and System Safety*, Vol. 92, 2007, pp. 957–960.

31. Mullershon, H., and Liebsher, M., "Statistics and Non-Linear Sensitivity Analysis with LS–OPT and DSPEX," Proceedings of the10th International LS–DYNA Users Conference, Dearborn, MI, 8–10 June 2008, pp. 4-1 and 4-13.

32. Homma, T, and Saltelli, A., "Importance Measures in Global Sensitivity Analysis of Nonlinear Models." *Reliability Engineering and System Safety* Vol. 52, 1996, pp. 1–17.

33. Sudret, B., "Global Sensitivity Analysis Using Polynomial Chaos Expansion," *Reliability Engineering and System Safety*, Vol. 93, 2008, pp. 964–979.

34. Mullur, A. and Messac, A., "Extended Radial Basis Functions: More Flexible and Effective Metamodeling," *AIAA Journal*, Vol. 43, No. 6, June 2005, pp. 1306–1315.

35. Mullur, A. and Messac, A., "Metamodeling Using Extended Radial Basis Functions: A Comparative Approach," *Engineering with Computers*,Vol. 21, 2006, pp. 203–217.

36. Anderson, M. C., Gan, W., and Hasselman, T. K., "Statistical Analysis of Modeling Uncertainty and Predictive Accuracy for Nonlinear Finite Element Models," Proceedings of the 69th Shock and Vibration Symposium, Minneapolis/St. Paul, MN, 1998.

37. Horta, L. G., Lyle, K. H., Lessard, W. B., "Evaluation of Singular Value Decomposition Approach for Impact Dynamic Data Correlation," NASA TM 2003–212657, October 2003.

38. Regis, R. G., and Shoemaker, C. A., "Constrained Global Optimization of Expensive Black Box Functions Using Radial Basis Functions," *Journal of Global Optimization*, Vol. 31, September 2005, pp. 153–171.

REPORT DOCUMENTATION PAGE

Form Approved
OMB No. 0704-0188

1. REPORT DATE *(DD-MM-YYYY)*	2. REPORT TYPE	3. DATES COVERED *(From - To)*
01- 11 - 2012	Technical Memorandum	

4. TITLE AND SUBTITLE

Development and Calibration of a System-Integrated Rotorcraft Finite Element Model for Impact Scenarios

5a. CONTRACT NUMBER

5b. GRANT NUMBER

5c. PROGRAM ELEMENT NUMBER

6. AUTHOR(S)

Martin, Annett S.; Horta, Lucas G.; Jackson, Karen E.; Polanco, Michael A.; Littell, Justin D.

5d. PROJECT NUMBER

5e. TASK NUMBER

5f. WORK UNIT NUMBER

877868.02.07.07.05.02.01

7. PERFORMING ORGANIZATION NAME(S) AND ADDRESS(ES)

NASA Langley Research Center
Hampton, VA 23681-2199

8. PERFORMING ORGANIZATION REPORT NUMBER

L-20199

9. SPONSORING/MONITORING AGENCY NAME(S) AND ADDRESS(ES)

National Aeronautics and Space Administration
Washington, DC 20546-0001

10. SPONSOR/MONITOR'S ACRONYM(S)

NASA

11. SPONSOR/MONITOR'S REPORT NUMBER(S)

NASA/TM-2012-217785

12. DISTRIBUTION/AVAILABILITY STATEMENT

Unclassified - Unlimited
Subject Category 39
Availability: NASA CASI (443) 757-5802

13. SUPPLEMENTARY NOTES

14. ABSTRACT

Limited to 200 words.

15. SUBJECT TERMS

Composites; Crashworthiness; Energy absorption; Finite element method; Impact loads; Rotary wing aircraft

16. SECURITY CLASSIFICATION OF:			17. LIMITATION OF ABSTRACT	18. NUMBER OF PAGES	19a. NAME OF RESPONSIBLE PERSON
a. REPORT	b. ABSTRACT	c. THIS PAGE			STI Help Desk (email: help@sti.nasa.gov)
					19b. TELEPHONE NUMBER *(Include area code)*
U	U	U	UU	63	(443) 757-5802